LUND UNIVERSITY

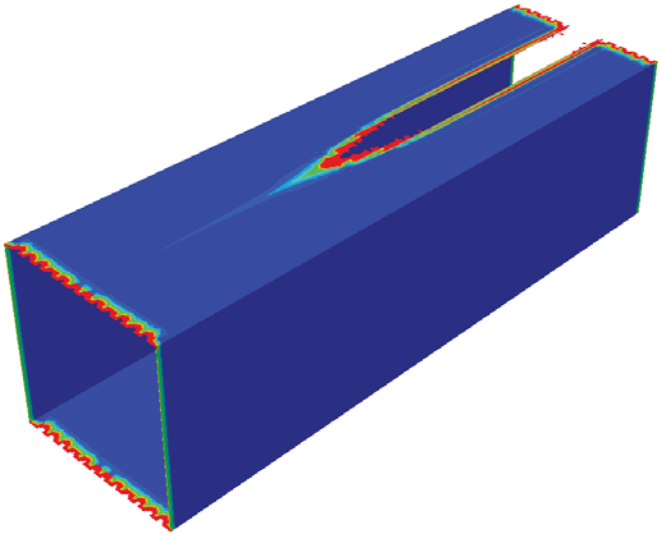

ANALYSIS AND DESIGN OF AN ADHESIVE JOINT IN WIND TURBINE BLADES

JONATAN PETTERSSON

Structural Mechanics

Master's Dissertation

DEPARTMENT OF CONSTRUCTION SCIENCES

DIVISION OF STRUCTURAL MECHANICS

ISRN LUTVDG/TVSM--16/5217--SE (1-72) | ISSN 0281-6679

MASTER'S DISSERTATION

ANALYSIS AND DESIGN OF AN ADHESIVE JOINT IN WIND TURBINE BLADES

JONATAN PETTERSSON

Supervisor: Professor **KENT PERSSON**, Div. of Structural Mechanics, LTH.

Examiner: Professor **PER-ERIK AUSTRELL**, Div. of Structural Mechanics, LTH.

Printed by Media-Tryck LU, Lund, Sweden, July 2016 *(Pl)*.

For information, address:
Division of Structural Mechanics,
Faculty of Engineering LTH, Lund University, Box 118, SE-221 00 Lund, Sweden.
Homepage: www.byggmek.lth.se

Abstract

The demand for renewable energy is constantly increasing and in order to compete with other sources of energy the wind energy output has to increase. The power output from wind turbines are highly dependent on the swept radius of rotor blades. Increasing the length of the rotor blades will increase the weight of the blades, resulting in higher demands of the structural performance, but also introducing transportation issues. This has introduced the need for a lightweight blade structure which can be constructed in modules and then assembled at the site of construction. Such modular design requires high attention to the details of connections to make the structural performance desirable during its life time.

A proposed design for such a connection was studied with regard to stress concentrations when subjected to normal tensile stresses. The design was also optimized to utilize the material better by varying certain parameters to distribute the general stress level more evenly over the entire structure and avoiding local stress concentrations at the connection.

The optimum design was further investigated by considering failure in the adhesive material. Two different types of epoxy adhesives, one brittle and one ductile, were compared in terms of load capacity. A parametric study was also conducted to investigate in detail how different failure properties of the adhesive material will affect this load capacity.

It was shown that the investigated adhesive joint should be designed such that abrupt stiffness changes in the connection are minimized and transitions are made smoothly. It was also determined that a more ductile adhesive with a somewhat lower failure strength will yield a stronger joint than a more brittle adhesive with higher stiffness and strength.

Acknowledgements

This master's dissertation concludes my five years at Lund University and my Master's degree in Structural- and Civil engineering. The work was conducted at Winfoors office in Lund and the paper was published by The Division of Structural Mechanics at Lund University Faculty of Engineering.

I would like to thank Professor Kent Persson for supervising my work and guiding me through this process. Furthermore, I would like to thank my colleagues at Winfoor for their company during this period. Last but not least I would like to thank my friends and family for their support during this thesis and my education.

Jonatan Pettersson, Lund, June 2016

Contents

List of Figures

List of Tables

1
Introduction

1.1 Background

The demand for renewable energy is constantly increasing which has resulted in a significant increase of the amount of power output produced by wind energy. Since the beginning of the 21st century there has been an exponential increase of the total installed capacity of wind power world wide [10]. This demand is expected to keep increasing which puts a lot of demand in creating larger wind turbines that can produce more energy. The power output from a wind turbine is linearly increasing with the rotor swept area [4] which is why a lot of research is put into developing longer blades. An increase of blade length, however, results in a large weight increase and transportation issues

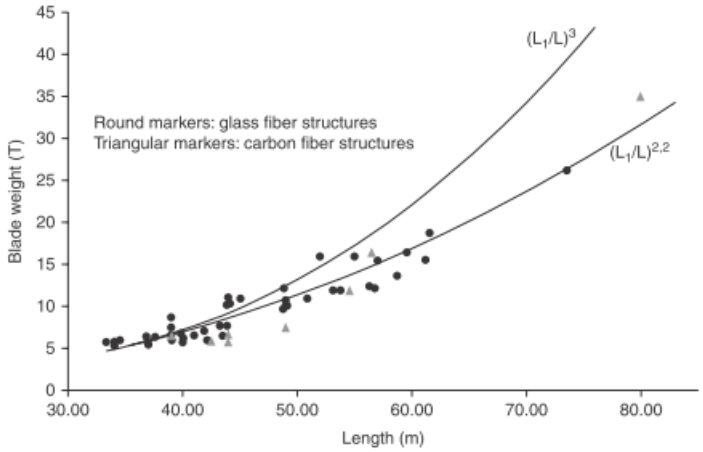

Figure 1.1: Increase of weight in wind turbine blades as a function of length [3]

Figure 1.1 shows historical data of how the weight of wind turbine blades has increased with the length. It suggests that the weight increases with the length to the power of 2.2 instead of to the power of 3 as earlier suggested [3]. This is due to technological advances in aerodynamic- and structural design of the blades. This relationship, however, can probably be further reduced. From Figure 1.1 it can also be noted that most structures are made out of glass fibre reinforced polymers (GFRP) and only a few are made of carbon fibre reinforced polymers (CFRP). CFRP can be of advantageous use since these provide higher stiffness, strength and better fatigue properties than GFRP [24]. The latter one, however, is most widely used in wind turbine blade design due to its low cost. An increase use of carbon fibre could

therefore be used to reduce the increased weight as a function of increased length. Another issue that arise when the blade length is increased is the transportation issues. The cost of transportation is around 8% of the total cost of a wind project [10]. This includes all parts such as turbine, blades and towers. An increased length of the blades, however, can be assumed to form a substantial increase of this cost. In addition to the cost, land-based wind turbines will be limited in how long the blades can be in order to make transportation physically possible.

In order to overcome these obstacles Winfoor are in the process of developing a new type of wind turbine blade called the Triblade. The Triblade technology aims to both reduce the self-weight of the blade by incorporating CFRP in the entire blade but also by reducing the amount of used material by having three smaller blades in a triangular configuration connected with a truss structure. The principal design of the lightweight structure is shown in Figure 1.2.

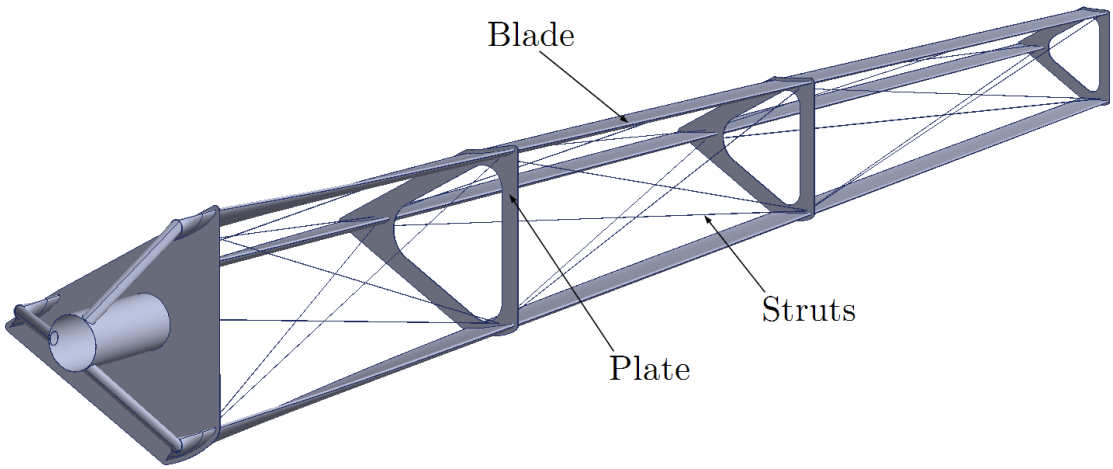

Figure 1.2: Example prototype CAD drawing of the Triblade. Courtesy of Winfoor.

The Triblade technology also aims to manufacture the blade in pultruded sections between each plate and assemble the structure at the location of erection to further decrease the cost as well as ease of transportation. A modular design like this requires strong connections between the sections of the blades in order to withstand the acting forces.

A prototype of this connection without taking the struts into account have been manufactured by the carbon fibre manufacturer Marström. They have previous experience from the marine industry and the assembly of compressed sailboat masts. Their experience serves as the base for the prototype design where one component is inserted into the other with a certain overlapping technique and then joined together with adhesives.

Former thesis work at Winfoor have focused on the structural behaviour of the entire truss structure with regard to buckling and dynamic analysis etc. [20].

1.2 Aims and objectives

The aim of this master thesis is to develop an efficient design of the adhesive joint where structural elements are connected using an overlap as suggested by Marström. In addition, the aim is also to develop the methodology for this design process and how this can be performed in an optimum manner.

The aims of the thesis is reached through a number of objectives:

- Develop a numerical model of the joint design.
- Perform parameter studies regarding the geometrical properties of the connected elements.
- Determine an efficient geometry of the connection from the results from the parameter study.
- Determine which parameters of the adhesive material that is of largest importance and how these can be varied to provide the strongest joint design.

The work will contribute to knowledge not only for Winfoor in how they can connect their parts, but will also add knowledge in large about adhesive connection of carbon fibre components.

1.3 Limitations

- Only one specific connection and corresponding load case was considered when determining the load case used in the analysis.
- The carbon fibre was analysed on a structural level, i.e. no consideration is taken to to individual bonding of laminates, delamination, etc.
- Failure and damage in the carbon fibre material was not considered.
- No experimental investigations were made.

1.4 Outline

Chapter 1:	Introduction	Describes the background-, aim-, objective- and limitations of the thesis.
Chapter 2:	Materials	Chapter describing the materials used in the connection.
Chapter 3:	Wind Turbine Technology and the Triblade Technology	Chapter describing traditional wind turbine technology and design as well as the Triblade technology, the manufactured prototype and forces acting on the connection.
Chapter 4:	Theory	Theory chapter describing the basic theories of fracture mechanics, the finite element method and element types used in the scope of this thesis.
Chapter 5:	Analysis of the Overlapping Design	The proposed connection technique is analysed by considering several parametric studies and an optimum design is proposed.
Chapter 6:	Analysis of Failure in the Overlapping Design	Failure in the connection is analysed by considering different adhesive properties in order to achieve a joint with high load capacity.
Chapter 7:	Final Remarks	Conclusions from the thesis and suggestions for further work.
	Bibliography	Reference list of literature used for the thesis.

2
Materials

2.1 Fibre Reinforced Polymers, FRP

Fibre Reinforced Polymers, denoted as FRP, belongs to a material group more widely referred to as composites. A composite material consists of at least two or more materials that can be distinctly separable by chemical or mechanical properties [7]. A composite material usually consists of the three components; reinforcement, matrix and interface as seen in Figure 2.1. The reinforcement is a discontinuous material embedded in a continuous matrix material whereas the interface acts as a bond between the reinforcement and the matrix. The properties of a composite material is therefore dependent on numerous factors. This can include the orientation and direction of the reinforcement, constitutive properties of the materials as well as the bonding between reinforcement and matrix.

In FRP specifically, the reinforcement used is some type of fibrous material while polymers constitutes the matrix phase. Among these fibrous reinforcement material glass- and carbon fibre are the most widely used. Glass fibre, GFRP, is usually chosen because of its low cost while carbon fibre, CFRP, is most often used when there are special requirements of the strength,stiffness and weight of the structure. Due to the special requirements of the Triblade structure carbon fibre composites are mainly in the scope of this thesis work.

2.1.1 Carbon Fibre Reinforced Polymers, CFRP

Carbon fibres can be characterized by anisotropic material properties where the fibre in the longitudinal direction possess much higher strength and stiffness than in the transverse direction. The longitudinal stiffness ranges from 250-390 GPa while the transverse stiffness ranges from 12-20 GPa [7]. The direction of the reinforcement, in this case the fibres, within the matrix component will therefore have a large impact on the specific properties of the composite material.

As seen in Figure 2.1 the constituents of carbon fibre, interface and matrix constitutes a lamina layer, also denoted ply. Several plies bonded together will constitute the actual material properties used in the structural analysis. It should be noted that the direction of fibres can differ between plies in order to change the properties of the material. The material properties for a ply with a certain fibre direction can theoretically be determined using the rule of mixture. This method takes into account both the stiffness of the matrix phase as well as the fibrous reinforcement

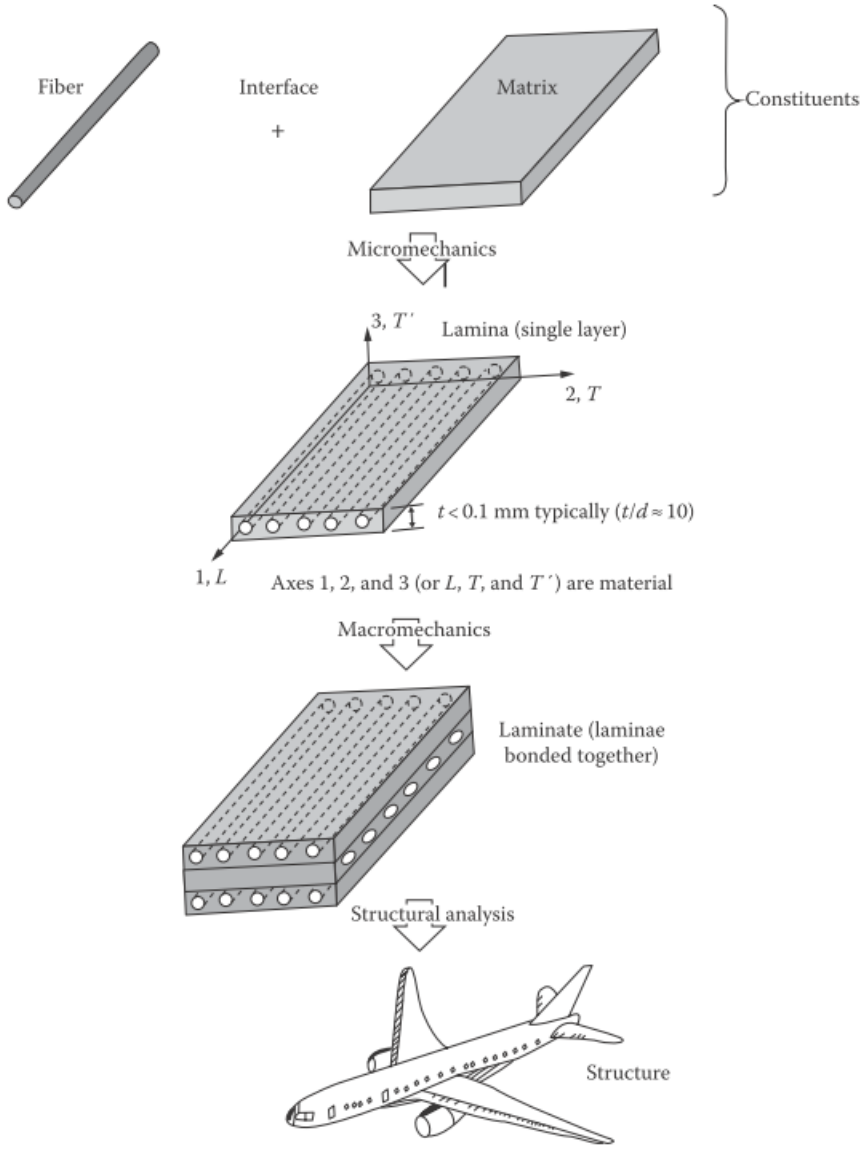

Figure 2.1: Levels of analysis for composite materials from the individual constituents to the structural analysis [8]

material to calculate material properties such as the longitudinal elastic modulus as well as the major Poisson's ratio (the larger value of the Poisson's ratio) [8]. The details of this method however is not included in this thesis.

Both the individual direction of fibres in each ply as well as the number of plies can be varied in a number of ways in order to obtain different constitutive behaviours. Each ply is usually given as a preconstructed mat where the fibres are given in one specific direction (unidirectional mat) or in several as a weaved pattern. For example it is common to have a weaved mat where the fibres are located in the 0° and 90° direction. If this type of mat is combined with a mat having fibres in the +45° and -45° direction such that the amount of fibres in all of these directions are the same, the constituent behavior of the complete laminate could be considered

quasi-isotropic. That is, the in-plane response is the same in all directions.

Most if the orientation combinations, however, will result in a strictly orthotropic behaviour where 9 independent engineering constants are needed to describe the constituent behaviour. This is usually not needed, however, since laminates usually are rather thin compared to the in-plane dimensions and the fibres are oriented in this plane. Plane stress conditions can therefore be assumed when considering the stress-strain relationship [8]. The orthotropic elastic stress-strain relationship for plane stress conditions are given in Equation 2.1 where only 4 independent constants are required to determine the constitutive relationship [22].

$$\begin{bmatrix} \varepsilon_1 \\ \varepsilon_2 \\ \gamma_{12} \end{bmatrix} = \begin{bmatrix} 1/E_1 & -\nu_{12}/E_1 & 0 \\ -\nu_{12}/E_1 & 1/E_2 & 0 \\ 0 & 0 & 1/G_{12} \end{bmatrix} \begin{bmatrix} \sigma_1 \\ \sigma_2 \\ \tau_{12} \end{bmatrix} \tag{2.1}$$

2.2 Adhesives

An adhesive material can be defined as a substance applied between two surfaces and creating a bond to each of these surfaces. The final result is then composed by two different sections that are bonded together such that mechanical forces can be transfered over this interface [6]. The forces that holds these two surfaces together can arise from van der Waals forces, chemical bonding, electrostatic attraction and mechanical entanglement.

In composite materials, adhesives can be used both to bond together different laminate components but also as the matrix material used to bond together the individual fibrous reinforcement as described in Section 2.1

The parts joined together by an adhesive material are called adherends. Stresses can be transferred between these adherends in a much more uniform way and at lower weight than if mechanical fasteners such as bolts or nails were to be used. Due to this uniform distribution adhesive bonds even stronger than the adherends can be created. Other advantages compared to mechanical fasteners include for example better resistance to fatigue loading, reduced cost and low weight. Disadvantages are the controlled environment needed in order to get a good bonding with regard to curing time, surface preparation, pressure, temperature etc. as well as difficulties regarding visual examination of the joint during the service life.

An adhesive material usually consists of several components in order to get the specific properties needed for the adhesive. Such components includes the adhesive base which has the function to form the bond and is the main component of the adhesive. Other components can be added to modify the properties of the adhesive and could include hardeners to speed up the reaction time at curing, solvents and diluents to change the viscosity as well as fillers to change properties such as strength, fracture toughness, thermal expansion, thermal and electrical conductivity, heat resistance, shrinkage, etc.

Adhesives can be classified into natural and synthetic adhesives. A natural adhesive could be vegetable- or animal-based while a synthetic adhesive is based of hydrocarbon and can be subdivided into thermosetting-, thermoplastic- and elastomeric adhesives or a combination of them called adhesive alloys. Synthetic adhesives are commonly used for structural applications. Such an adhesive is the epoxy adhesive which is usually used as a matrix material in composite materials but also used to join different components together.

2.2.1 Epoxy adhesives

Epoxy adhesives are the most widely used thermosetting adhesive under the synthetic group of adhesives described above. Thermosetting adhesives can, after curing, not be melted again due to cross-links created during this process. Curing occurs due to chemical reactions and can be done both in room temperature and at higher temperatures. Additional pressure might also be needed during curing for some thermosettings.

Epoxies are available both as a one-part system as well as a two-part system. The one-part system usually solely consist of the adhesive base while for a two-part system a hardener is added which enables faster curing at lower temperatures. When cured, this type of adhesive will provide a stiff joint with low elastic deformation and good resistance to heat. It can be used for most types of adherends and are mostly used for stressed joints.

2.2.2 Adhesive joint designs

There are a number of ways in which an adhesive joint design could be produced. Some examples of adhesive joint designs together with a small description are given in Figure 2.2.

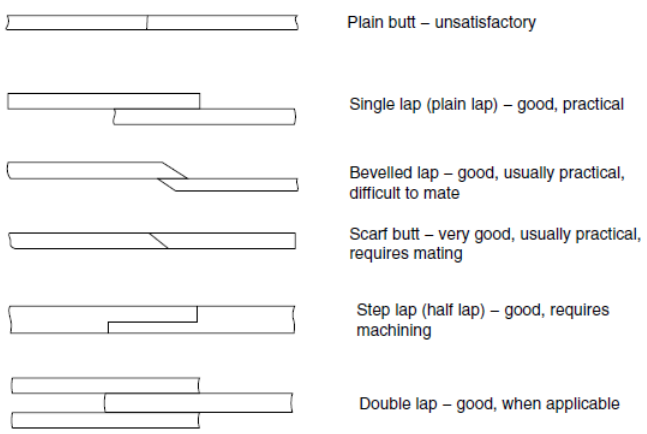

Figure 2.2: Some examples of adhesive joint designs [6].

3

Wind Turbine Technology and the Triblade technology

3.1 Traditional wind turbine blade design

When designing wind turbine blades both aerodynamic and structural design needs to be considered. The blade needs to be aerodynamically optimized in order to produce the maximum energy output. The aerodynamic loading in turn will affect the design of the blade structure. In order to design wind turbine blades both of these components needs to be considered simultaneously. Some basic theory of aerodynamics is discussed here in order to explain relevant aerodynamic loads acting on the blade. It should be noted that this section only includes the design of wind turbine blades for horizontal-axis wind turbines (HAWT).

3.1.1 Aerodynamic design

The main goal of HAWT is to transform the wind energy acting on the rotor blades into kinetic energy. The wind pressure acting on the blades therefore needs to induce a rotational force causing the blades to rotate. In order to maximize the induced rotational force due to the wind pressure on the blades an airfoil shape of the wind turbine blade is used. Airfoil shapes have numerous application areas and are, in addition to wind turbine blades, used in aircrafts, propellers etc. and will produce an aerodynamic force when moved through a fluid such as air. Different shapes of the airfoil works better for different applications but the general concept can be seen in Figure 3.1.

Figure 3.1 shows the relative wind speed, V_{rel}, coming in with a certain angle of attack, α, towards the leading edge (thicker edge) of the airfoil. The resulting force on the airfoil due to this relative wind will be composed of a lift and a drag force. The lift force, F_L, will act in a direction perpendicular to the relative wind while the drag force, F_D acts in the relative wind direction. The rotational force on the rotor will then be the sum of the lift- and drag force components acting in the direction of the rotor plane. Thus, the idea of an airfoil is that the lift force is significantly larger than the drag force in order to produce a rotational force. The component of the force acting in the direction of the rotor axis is denoted thrust force and are in general significantly larger than the rotational force.

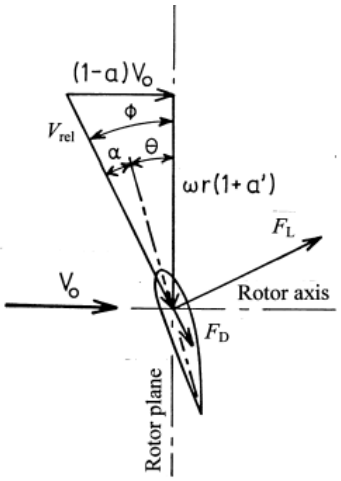

Figure 3.1: The general concept of a HAWT airfoil where the incoming wind will produce lift and drag forces [26]

The relative wind direction, V_{rel} is different from the incoming wind direction, denoted V_0 in Figure 3.1 since the rotor is turning with high speed. When the incoming wind passes through the rotor plane an interaction with the moving rotor blade will occur and an additional wind velocity acting in the perpendicular direction to the incoming wind is induced [26]. The additional wind velocity is dependent on the speed of the blade at this particular location along the blade axis. Since the velocity of the blade in the tangential direction increases along the blade axis, a larger additional wind velocity is induced at the tip of the blade compared to the root. The relative wind direction will therefore vary along the blade's axis and a twist in the blade is introduced to maximize the efficiency of the blade. This twist is called pitch angle which can be seen as the angle between the rotor plane and the chord line (the straight line moving through the trailing- and leading edge of the airfoil) denoted Θ in Figure 3.1.

The generation of lift force can be explained by the airfoil creating a streamline of wind around the upper- and lower side of the airfoil [9]. Higher pressure is generated on the lower side and lower pressure is generated on the upper side. The pressure difference generated between the upper- and lower side will in turn generate the lift force acting on the airfoil as seen in Figure 3.2.

The flow of wind through the plane of a wind turbine rotor is very complex and will depend on a lot of different variables. The prediction of such behaviours can be made with very advance three dimensional fluid dynamics calculations which requires large computational means but also in a much simplified manner using the Blade Element Momentum method (BEM method) [3]. Such methods are used in the aerodynamic design process in order to optimize the power output. The BEM method can vary from being used in a very simplified 1-D manner where the air flowing through the rotor plane is assumed to behave in the same manner at all given points along the axis to the more advanced model where the blade is discretized in a finite number of elements along the blade axis. The theory used for the simplified

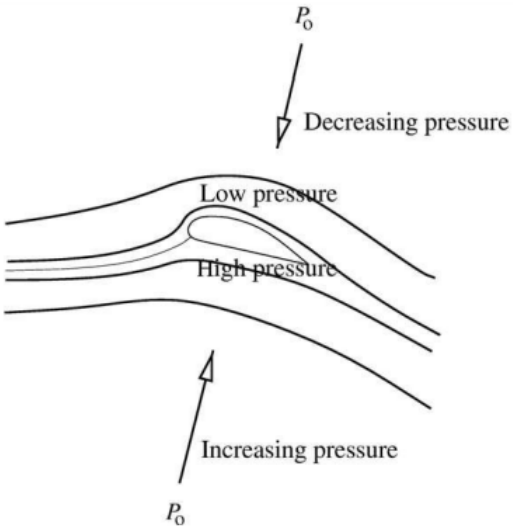

Figure 3.2: Higher pressure on the lower side of the airfoil than on the upper side explains the generation of lift [9].

case is then used for all of these elements [3].

The BEM method is used for the Triblade to determine an initial design at relatively low computational cost. With a given blade length and wind speed the geometric properties such as chord length and pitch angle, thrust- and rotational forces can be calculated along the blade's axis with optimum power output as the basis of design. There is, however, many details that are not accounted for by using the BEM theory. A more refined aerodynamic design requires more advanced CFD-calculations.

3.1.2 Structural design

The structure of traditional blades usually consists of a hollow core with an external shape determined by considering the desirable aerodynamic properties. Shear webs between the bottom and top of this hollow core is also incorporated in order to increase the stiffness and add shear resistance to the structure [4]. In addition, some extra stiffness is usually incorporated in the shell around the webs to increase the bending stiffness. This area is called a spar cap and act as flanges used in traditional I-beams to increase bending stiffness.

The shear web and spar caps combined can be seen as different beam elements depending on the number of webs and how these interact with each other. If one shear web is incorporated the main structural component could be viewed as an I-beam while if two webs are incorporated it could be viewed as a closed rectangular cross section denoted a box spar. The shear web and spar caps constitutes the main structural components of wind turbine blades while the air foil shape is mainly determined due to desirable aerodynamic properties. Figure 3.3 shows a principal sketch with a simplified airfoil showing both a structure with one shear web and

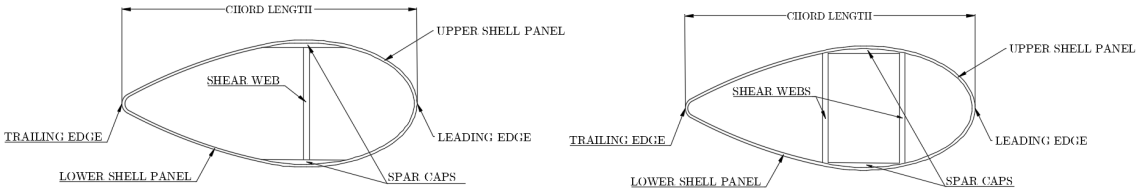

(a) One shear web.

(b) Two shear webs

Figure 3.3: Sketches showing the principal structural parts of a wind turbine blade with a simplified airfoil shape. (a) A core structure similar to an I-beam with only one shear web, (b) A rectangular cross-section core with two shear webs.

one with two webs, creating a rectangular box cross section as a core in the blade. Additional blade terminology can also be seen in this figure such as chord length, shell panels, leading edge and trailing edge.

3.1.3 Additional loads

In addition to the aerodynamic loads such as thrust and rotational forces described in Section 3.1.1 wind turbine blades will also be subjected to gravitational loads due to the self-weight as well as centrifugal loads related to the rotation of the blades. The centrifugal loads are, as well as the gravitational loads, mass dependent. In addition to the mass, centrifugal forces acting on a wind turbine blade will also be dependent on the angular velocity together with with the radial distance to the rotational center. The centrifugal forces acting on a blade will act as a tensile force and can at a distance, r^*, from the blade root be calculated through Equation 3.1 [4].

$$F_c = \omega^2 \int_{r^*}^{R} m(r) r \mathrm{d}r \tag{3.1}$$

Where $m(r)$ is the mass dependent of the location along the blade's axis, r is the radial distance from the root, ω is the angular rotor speed [rad/s] and R is the length of the rotor blade. The angular rotor speed can be calculated through Equation 3.2 [25] where V_{hub} is the wind speed at the hub height, λ is the tip speed ratio (ratio between the tip speed of the blade and the wind speed at the hub height) and R is the radius of the rotor blade.

$$\omega = \frac{V_{hub}\lambda}{R} \tag{3.2}$$

The gravitational loads acting on a blade is simply calculated as the mass of the blade multiplied with the gravitational constant as seen in Equation 3.3.

$$F_g = \int_0^R m(r) g \mathrm{d}r \tag{3.3}$$

The gravitational force acting on a blade will always act in the center of mass in a direction towards earth's gravitational center and will therefore vary as the wind turbine blades are rotating. Centrifugal forces, however, will always act in an radially outward direction in the rotational plane. These forces and their acting direction are shown in Figure 3.4.

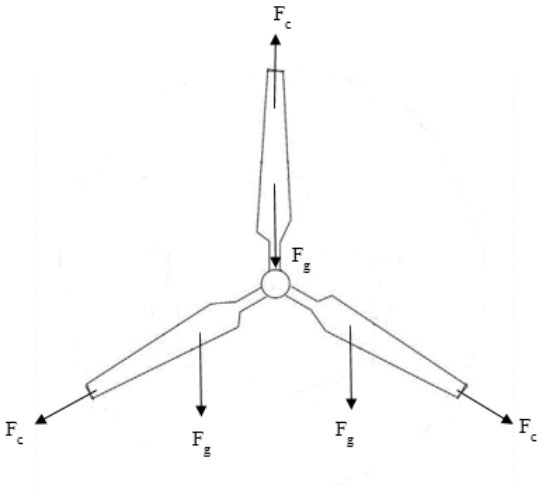

Figure 3.4: Centrifugal and gravitation forces acting on a HAWT.

3.2 The Triblade technology and previous work at Winfoor

The Triblade employs the main structural components as described in Section 3.1.2 for each individual blade. As opposed to traditional blades where each blade consist of one airfoil shaped blade, each blade of the Triblade will instead incorporate three airfoil shaped blades in a triangular configuration. Each of these individual blades will twist along the blade's axis in order to meet the aerodynamic requirements. Along the longitudinal axis the blade is divided into a number of subsections separated by plates that holds the triangular configuration in place. A truss configuration is incorporated between these plates and the individual blades in order to increase to the stiffness of the entire blade structure. The basis of this design can be seen in Figure 3.5

One of the main goals of the Triblade technology is to implement a modular design of the blades meaning that they are to be manufactured in smaller parts and then assembled at the construction site. In addition, it is desired to achieve an automatized manufacturing process with the use of pultrusion technique. By using pultrusion technique one is limited to manufacturing sections with a constant cross section. With modular design and pultrusion techniques as the basis of design it appears reasonable to manufacture each subsection of the blade between the plates

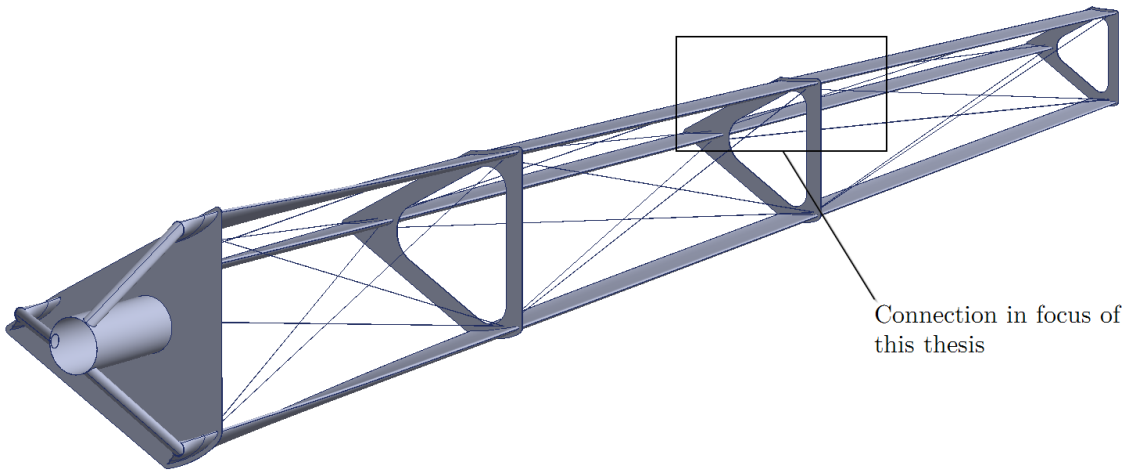

Figure 3.5: The connection in the scope of this thesis shown in a principal CAD drawing of the Triblade.

with constant cross section as individual parts and then using the plates as a connection point for assembling different subsections. The design of this connection is the main focus in the scope of this thesis and can be seen in Figure 3.5.

The design of this connection is in progress at Winfoor and in cooperation with the carbon fibre manufacturer Marström they are involved in a project to design this joint. Marström have previous experience in assembling similar carbon fibre components used in sail boat masts. Their experience is used as a first basis of design for connecting the individual blade components through the plate. The technique uses an overlapping section where the main structural parts, in this case the box spar of each blade, are joined together by inserting one part into the other and using an adhesive layer between the structural components. This joint design shows a big resemblance to the single lap joint shown in Figure 2.2 but for an entire rectangular cross-section.

3.2.1 Prototype

A prototype of this connection has been manufactured by Marström and can be seen in Figure 3.6a. The prototype aims to visualize how one individual subsection of the Triblade can be connected to the next through one of the plates. The general shape, however, is very simplified and shows more similarities to a sailboat mast than an airfoil used for wind turbine blades. This shape is used in the prototype due to the cost of manufacturing since the manufacturer already possessed molds for making such shapes. Since the main structural behaviour of the blade is contained to the box spar, consisting of two shear webs and two spar caps creating a rectangular beam element, this shape was deemed sufficient for the purpose of this prototype. A CAD model of the prototype was also produced using measurements in the real prototype and can be seen in Figure 3.6b. The CAD model was used to efficiently visualize the different parts and dimensions of the prototype.

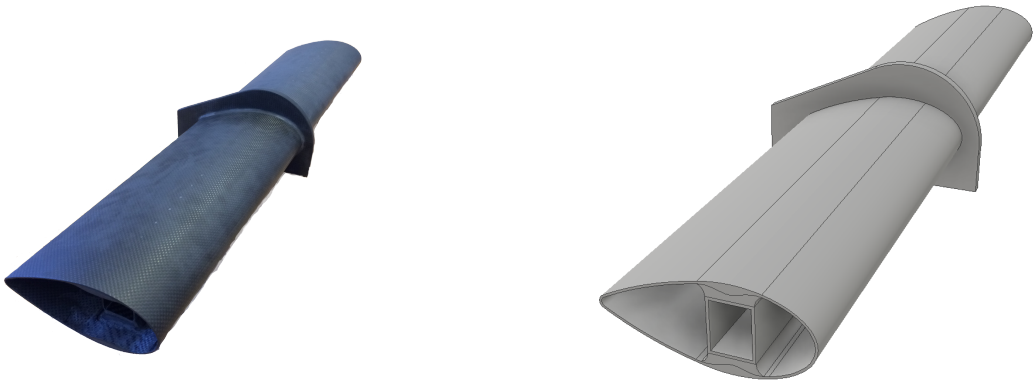

(a) Picture of the real prototype.

(b) CAD model of the prototype

Figure 3.6: Figure showing a picture of the real prototype together with a CAD model made from the prototype. (a) Real prototype, (b) CAD model of the prototype.

Geometry

The blades on both sides of the plate holds the same dimensions but are twisted by approximately 4.3 degrees in respect to each other to simulate the twist incorporated in the Triblade in order to maximize the aerodynamic efficiency. The cross-sectional dimensions of the blades are 210x90 mm where the larger dimension is the chord length and the smaller is the height of the blade. A sketch of this cross-section have been made from the CAD model and can be seen in Figure 3.7. The length of each blade is 0.5 m making the total length of the prototype approximately 1.0 m.

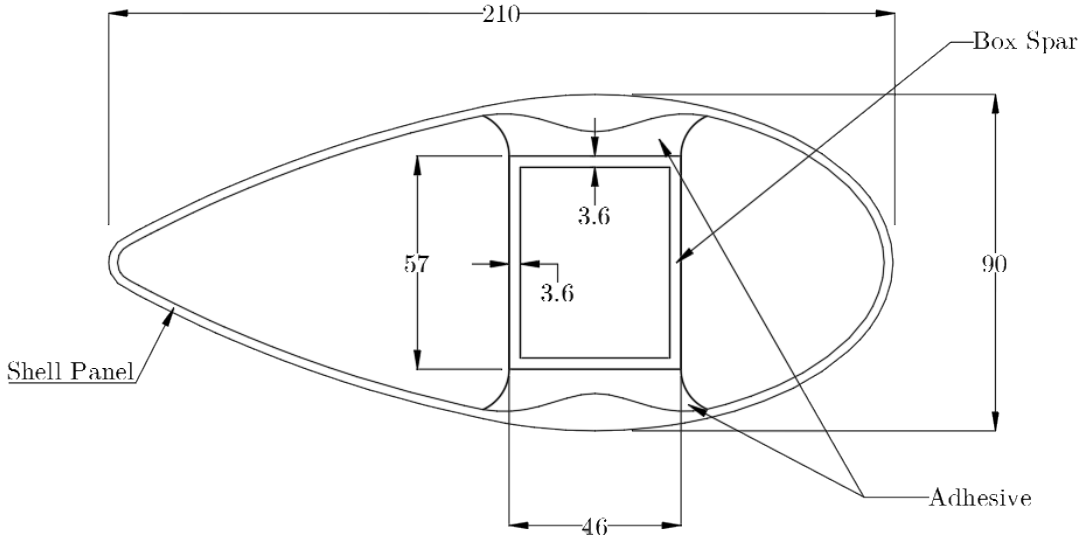

Figure 3.7: Sketch showing the blade cross-section of the prototype with dimensions in mm.

It should be noted that only the box spar in Figure 3.7 is of structural interest

and is used when connecting the blades through the plate. These connecting box spars are the investigated components in this thesis. The box spar of each blade continues through the plate overlapping each other where one of the spars is inserted into the other creating a single lap adhesive joint as seen in Figure 2.2. A conical shape of these box spars were also incorporated in order fit them together due to the dimensions and twist in respect to each other. The overlapping length is 0.15 meter on each side of the plate. A sketch of the overlapping section can be seen in Figure 3.8.

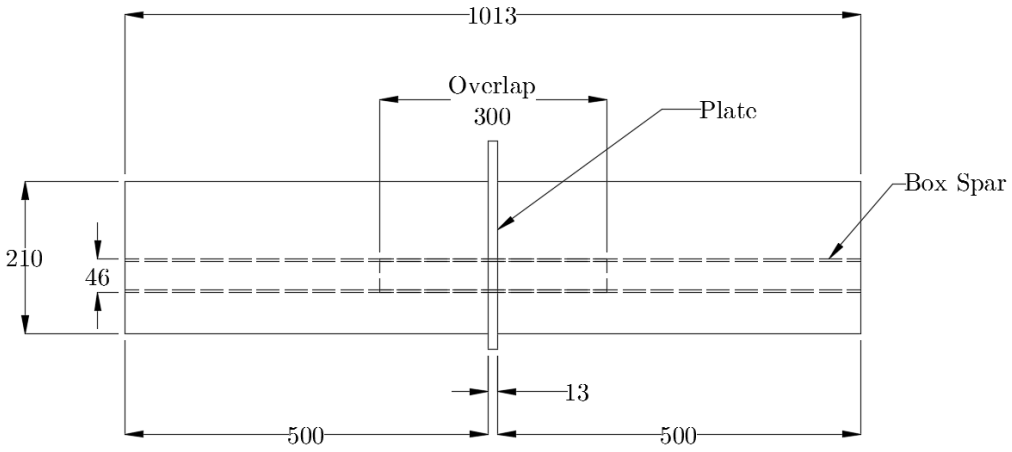

Figure 3.8: Sketch showing the prototype from above with the hidden box spar shown as dashed lined. Dimensions are shown in mm.

Material

The material employed in the prototype is carbon fibre for the main structural parts together with an adhesive used to bond different structural parts together. The manufacturing process together with the used material and mechanical properties have been obtained through communication with Marström AB.

Carbon fibre
When moulding the structural carbon fibre parts lamination of both unidirectional and weaved mats of carbon fibre were used. The unidirectional mat employs fibres only in one direction while the weaved mat used for this prototype have fibres located in the 0°-direction and in the 90°-direction, i.e. perpendicular to each other. The weaved mat will therefore exhibit similar mechanical properties in two directions. These types of mats have for the prototype been stacked in different combinations and number of layers in different parts of the prototype contributing to a varying structural behaviour over the part. As for all composite materials, as described in Section 2.1, the carbon fibre mats are contained in a matrix material creating the completed stiff, hardened laminate structure.

The different types of carbon fibre mats employed in the prototype together with the product name and in-plane mechanical properties can be seen in Table 3.1. The Poisson's ratio in this table has been assumed through similar material data from another carbon fibre manufacturer in order to fully describe the in-plane mechanical properties.[27].

Table 3.1: Carbon fibre properties given from Marström AB.

Carbon fibre	Unidirectional fibres 600 gr/m^2 Hexply M9.6 UD600	Weaved Fabric 0-90° 600 gr/m^2 Hexply M49 600 T2x2	Weaved Fabric 0-90° 285 gr/m^2 Hexply M49 285P
E_1	120 GPa	60 GPa	60 GPa
E_2	10 GPa	60 GPa	60 GPa
G_{12}	0.5 GPa	0.5 GPa	0.5 GPa
ν_{12}	0.3	0.1	0.1
Tensile Strength	1400 MPa	650 MPa	650 MPa
Compressive Strength	1000 MPa	650 MPa	650 MPa

The properties of two types of weaved fabric are given in Table 3.1 where the only difference is the amount of fibres contained within the mat measured in terms of grams/m^2. The mat weight is directly correlated to the thickness of the completed laminate. It can be assumed that 100 gram/m^2 carbon fibre corresponds to approximately 0.1 mm thickness in the completed laminate.

Adhesive and matrix material

The adhesive material used in the prototype to bond the components together and as matrix material is an epoxy with the product name 3M DP490 Epoxy. The mechanical properties for this adhesive at 23°C can be found in Table 3.2 [13], [28].

Table 3.2: Mechanical properties for 3M DP490 Epoxy

Adhesive	3M DP490 Epoxy
E	659.6 MPa
ν	0.38
G	239 MPa
Plastic Shear Strength	36.1 MPa

Material in the box spar

As stated in Section 3.2.1, the stacking combination and the number of laminates vary over the different structural parts in the prototype. It is only of interest, however, to show the layered stacking of the box spar since this is the main structural component and used to connect the blades through the plate. The individual layered stacking of laminates in different parts of the box spar can be seen in Figure 3.9..

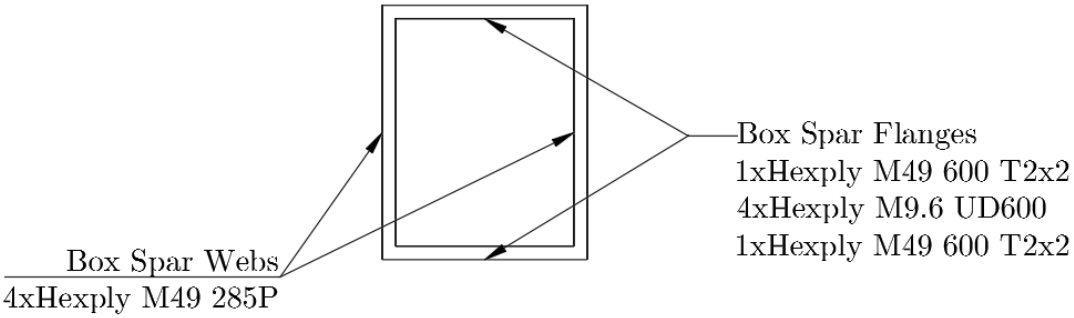

Figure 3.9: Cross-section of the box spar in the prototype and stacking of laminates in different parts.

3.3 Forces on the connection

To obtain good results from the numerical simulations and analyses of the connection, realistic forces need to be applied. These forces include aerodynamic-, gravitational and centrifugal forces as described in Section 3.1.3. Previous work at Winfoor includes the development of a Matlab script calculating the internal forces along each individual blade of the Triblade based on aerodynamic and gravitational forces. To calculate these forces the CALFEM toolbox developed at Lund University was used. The CALFEM toolbox employs numerical calculations according to the theories of the finite element method described in Section 4.2 to calculate these internal forces. The internal forces will depend on a number of variables such as the type of airfoil, chord- and blade length, pitch angle, number of subsections in the blade and if its pultruded.

To determine the forces, a connection at a specific location and type of Triblade needs to be considered. The prototype served as the basis for this decision. The aim was to find a certain connection on a Triblade with a certain length that was as geometrically similar to the prototype as possible. Since the geometrics of the prototype and the Triblade were highly different in some aspects, only one geometric component was considered. The most significant structural geometric property is the height of the blade since this will have a significant effect on the size of the box spar and hence the bending stiffness of the blade. It was also desirable that the pitch angle between the blades on each side of the plate was relatively close to the twisting between the blades in the prototype.

A connection that exhibits similar properties to those described in the paragraph above can be found in a 15 m long pultruded Triblade at the connection located 12 meter from the root. This blade is divided into five subsections where each subsection holds a constant cross-sectional area and pitch angle. The SG6043 airfoil is used for this blade where the width to height ratio is 8.46. The principal shape of this airfoil can be seen in Figure 3.10.
The cross-sectional geometric properties for the airfoil in each subsection of the 15

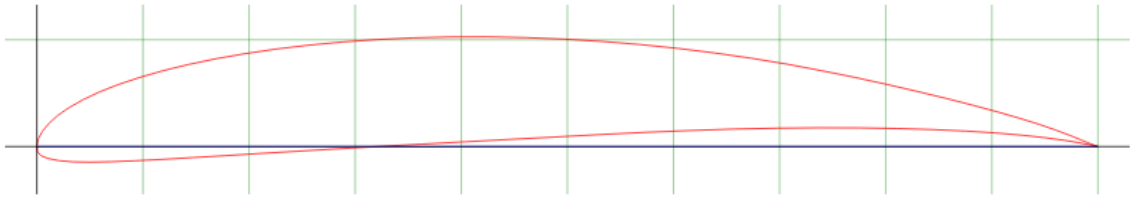

Figure 3.10: Principal sketch of the SG6043 airfoil with a width to height ratio of 8.46 [23].

meter blade can be seen in Table 3.3 and has been extracted from the CALFEM script. The connection of interest was found between subsection 4 and 5, i.e. 12 meter from the root of the rotor. With a blade height of approximately 95 mm at this point, this corresponds relatively well with the blade height of the prototype which is 90 mm. The connection at 12 meter from the root in a 15 meter long pultruded blade with a SG6043 airfoil has therefore acted as a reference connection when determining the loads acting on the connection.

Table 3.3: Table showing the properties of each subsection in the pultruded 15 meter Triblade.

Subsection	Length from hub [m]	Chord length [m]	Blade Height [m]	Twist angle [°]
1	0-3	1.0	0.118	26
2	3-6	1.0	0.118	13
3	6-9	1.0	0.118	10
4	9-12	0.8	0.095	6.5
5	12-15	0.8	0.095	5

3.3.1 Aerodynamic- and gravitational forces

The effects of aerodynamic- and gravitational forces were calculated as internal forces along the entire blade length for each individual blade in the Triblade configuration through the previously developed CALFEM script at Winfoor. The blade length was in the CALFEM script discretised into eight beam elements in each subsection of the blade yielding a total of 40 beam elements along each blade. The section forces at the beginning and end of each element were calculated through the element function `beam3s` [1]. The definition of orientations for these section forces are given from the function definition in the CALFEM manual as shown in Figure 3.11.

The local coordinate system for each blade element in the CALFEM script is defined as given in Figure 3.12 with the local y- and z-axis lying in the cross-sectional plane of the blade. The local x-axis follows the rotor blade axis from root to tip.

The calculated section forces for each connection in their respective individual blade, denoted blade 1, 2 and 3, are given in Figure 3.13.

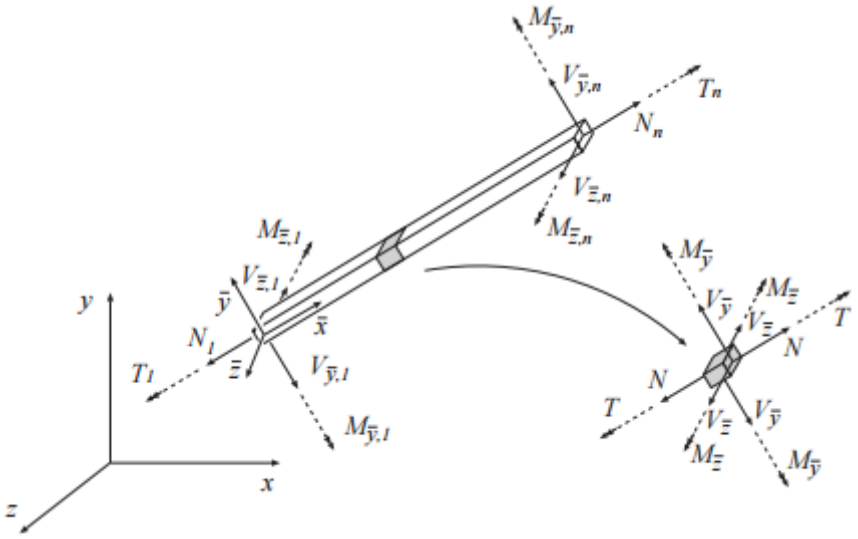

Figure 3.11: Definition of section forces for a three-dimensional beam element from the CALFEM manual [1].

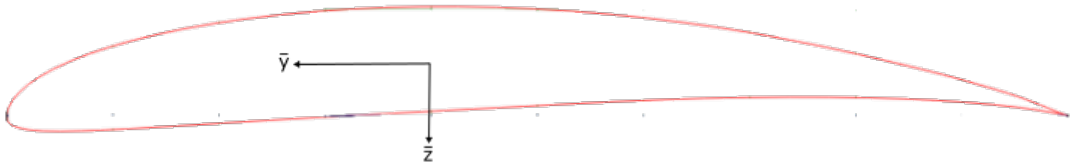

Figure 3.12: The local coordinate system of each beam element in `beam3s` for the cross-sectional plane.

3.3.2 Centrifugal forces

The centrifugal forces acting on the blade was not considered in the CALFEM script. The centrifugal force acting on the reference connection was therefore calculated in a simplified manner. A centrifugal force will induce a tensile force in the blade which will vary along the blade's axis ranging from a smallest value at the tip to the largest value at the root.

For the purpose of this simplified calculation no regard were taken to the plates and struts of the Triblade. Only the self-weight of each blade was considered and the centrifugal force was calculated as an additional normal force added to the previously calculated normal force in 3.13.

To calculate the centrifugal force at the connection the CALFEM script was used for extracting additional parameters. The cross-sectional area of the airfoil was simplified to an ellipse with a shell panel thickness of 2 mm. The outer dimensions of the ellipse were given from the chord length and blade height as given in Table 3.3 for each subsection. In addition to the airfoil shape the box spar with its internal dimensions also needed to be considered when calculating the self weight. Since the

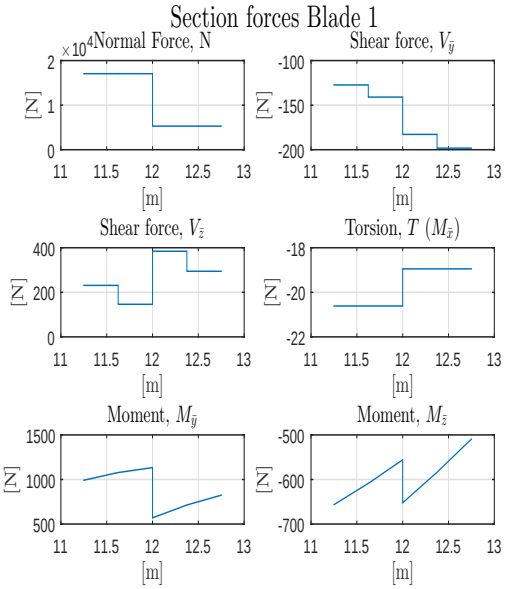

(a) Blade 1

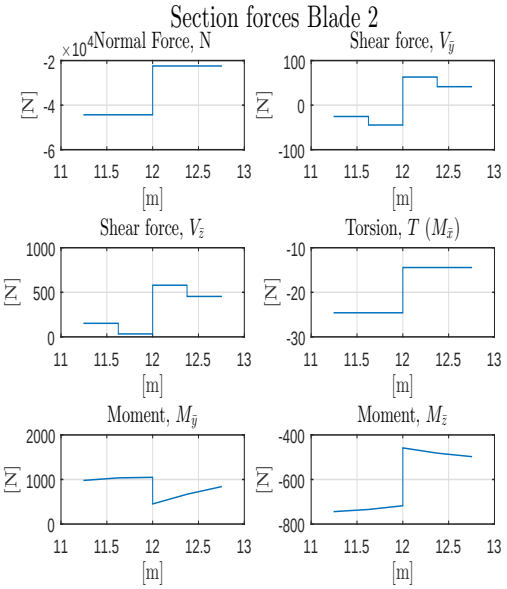

(b) Blade 2

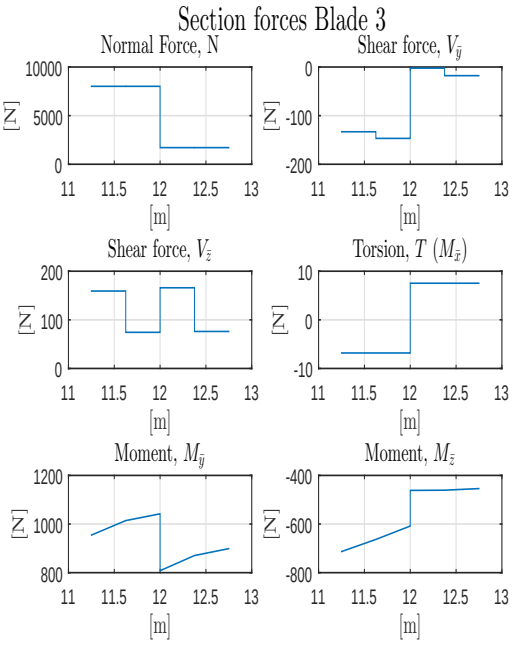

(c) Blade 3

Figure 3.13: Section forces around the connection at 12 meter for a 15 meter Triblade. (a) Blade 1, (b) Blade 2 and (c) Blade 3.

Table 3.4: Calculated values for the cross-sectional area of an individual blade based on simplifications

Subsection	Airfoil area [m^2]	Box spar area [m^2]	Total area
1	0.0035	0.0016	0.0051
2	0.0035	0.0016	0.0051
3	0.0035	0.0016	0.0051
4	0.0028	0.0013	0.0041
5	0.0028	0.0013	0.0041

width to height ratio for the box spar is not unambiguously determined a simple square shape was assumed. The height of this square shape was determined by subtracting the shell panel thickness from the blade height. As measured from the box spar in the Marström prototype, a thickness of 3.6 mm was assumed for the box spar. The simplified cross-sectional area for each subsection is summarized in Table 3.4.

When considering the reference connection at 12 meter from the root only the mass of the last subsection of the 15 meter Triblade will give rise to any centrifugal forces as described in Section 3.1.3. Since the cross-sectional area of this subsection is constant the centrifugal force acting on this connection can be calculated as given in Equation 3.4.

$$F_c = \omega^2 \int_{12}^{15} A\rho r dr \tag{3.4}$$

Where ω is the angular rotor speed, A is the area of subsection 5, ρ is the density of carbon fibre, assumed to 1600 kg/m^3 [27], and r is the integration variable in the interval between 12 and 15 meters. The angular rotor speed was calculated through Equation 3.2 with the assumption that the reference wind speed at the hub is 10 m/s and the tip speed ratio is 7 for optimal power output as commonly used at Winfoor. These values yielded an angular rotor speed of, $\omega \approx 4.7$ rad/s. The centrifugal force was then calculated through Equation 3.4 with inserted values as, $F_c = 5869$ N, at the connection of interest.

4
Theory

4.1 Fracture mechanics

Fracture mechanics is a field within mechanics with the purpose of predicting and studying the failure of solid materials due to crack initiation and crack propagation [19]. When damage occurs in a material fractures might grow and propagate due to stress concentrations at the crack tip. The longer the crack, the higher the stress concentration. Thus, the rate of crack propagation will increase with crack size and time [2]. This driving force at the crack tip can be expressed as a stress intensity factor or as available energy to the crack tip. The resistance to fracture is stated in terms of fracture toughness. The criteria for crack growth is then given by a balance between the crack tip loads and the fracture toughness.

The field of fracture mechanics can be divided into Linear Elastic Fracture Mechanics, henceforth denoted as LEFM and Non-Linear Fracture Mechanics, henceforth denoted as NLFM.

4.1.1 Modes of fracture

The stress concentrations at a crack tip can be divided into three components [21]. These are denoted Mode I, Mode II and Mode III. The directions of these stress field components are illustrated in Figure 4.1 [17].

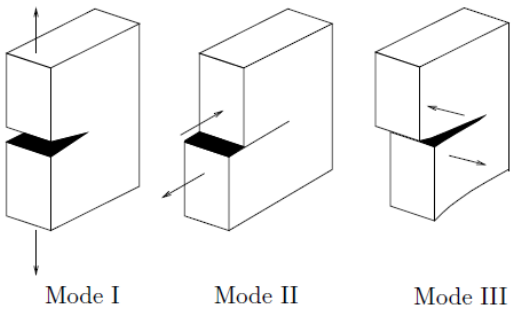

Figure 4.1: The three different modes of fracture. Mode I, Mode II and Mode III [17].

The three modes are according to Sun & Jin [19] described as one tensile mode in the normal direction of the crack and two shear modes in the plane of the fracture.

The first mode is the tensile opening mode and acts in the normal direction of the fracture. The second mode is a shear sliding mode acting in the same plane as the fracture perpendicular to the crack front. The third mode is a shear tearing mode also acting in the plane of the fracture but tearing over each other parallel to the crack front. In real-life problems a combination of the modes generally occurs [17] where a combination of Mode I and Mode II is most common.

4.1.2 Linear Elastic Fracture Mechanics, LEFM

LEFM is a field of fracture mechanics where the material response is assumed to be linear elastic. The crack growth and propagation is predicted using either an energy balance approach or by analytically determining the stress state at a crack tip with the use of a stress intensity factor. [17]. The Griffith's criteria is commonly used when considering an energy balance approach. The criteria states that a crack will grow when there is enough elastic energy stored in the body to create a new crack surface.

In reality, a plastic deformation zone will occur at the crack tip. The LEFM approach should therefore only be considered when this zone is small (Small Scale Yielding) and the plasticity can be disregarded.

Energy balance and the Griffith's criteria

The energy balance of a body is a key concept in fracture mechanics. It states that the amount of external mechanical energy supplied to a solid body per unit of time ($\dot{U}_e$) must be transferred into internal energy ($\dot{U}_i$), surface energy ($\dot{U}_s$), dissipated energy ($\dot{U}_d$) and kinetic energy ($\dot{U}_k$) as seen in Equation 4.1 [17].

$$\dot{U}_e = \dot{U}_i + \dot{U}_s + \dot{U}_d + \dot{U}_k \tag{4.1}$$

The internal energy is elastically stored energy which is a source of energy and can be moved to the left side. The surface energy is generated when a new surface emerges, i.e. when a crack grow. The dissipation is mainly due to friction and plasticity and will exhibit as a temperature change. The kinetic energy results from material velocity. The time derivative given in Equation 4.1 can instead be written as the derivative of a crack area, dA, to indicate changes in the system an can be seen in Equation 4.2

$$\frac{\partial \dot{U}_e}{\partial A} - \frac{\partial \dot{U}_i}{\partial A} = \frac{\partial \dot{U}_s}{\partial A} + \frac{\partial \dot{U}_k}{\partial A} + \frac{\partial \dot{U}_d}{\partial A} \tag{4.2}$$

In the 1920s, Griffith derived his energy balance approach based on Equation 4.2. The dissipation and kinetic energy were disregarded and all external and internal energy were assumed to be converted in to surface energy. Two variables was then introduced. The energy release rate, G, based on the difference in external and internal energy, i.e. the left hand side of Equation 4.2 and the crack resistance force,

R, based on the surface energy of the body, i.e the remaining part of the right hand side in Equation 4.2. Griffith's criterion then states that in order for a crack to grow, the energy release rate (the driving force for crack propagation) needs to reach a critical value and be equal to the crack resistance force. This is shown in Equation 4.3 where γ is the surface energy of the material. The factor of two for the surface energy is needed due to the fact that two new surfaces emerges when a crack grows.

$$G = R = 2\gamma \tag{4.3}$$

It can be shown that the energy release rate is a quadratic function of the crack length while the created surface energy is a linear function of the crack length. Thus, at a critical crack length propagation will occur rapidly and uncontrolled without increasing the applied stress. This is explained by the fact that the energy release rate that constitutes the driving force of crack growth will increase faster than the surface energy that is created, i.e. G becomes larger than R and Equation 4.3 is no longer in equilibrium. At this point total failure of the fracture will occur. A critical value of the energy release rate is therefore introduced and denoted G_c.

It should be noted that Griffith's criteria was derived from glass which is a brittle material. For brittle materials it has been shown that it is a reasonable assumption to disregard the dissipation and kinetic energy. When applying this energy criterion on ductile materials, however, plastic deformation at the crack tip needs to be accounted for and all sources of energy needs to be considered [2].

Stress Intensity Factor

Instead of considering the energy as the driving force of crack propagation as described in Section 4.1.2 this method considers the stress state near the tip of a sharp crack directly [16]. The approach states that the stress field for a given material point and specific load case can be calculated analytically through a stress intensity factor. If mode I loading as described in Section 4.1.1 is considered, the stresses acting in a specific point at a distance r and an angle θ from the crack tip can be described by Equation 4.4 [2].

$$\sigma_{ij} = \frac{K_I}{\sqrt{2\pi r}} f_{ij}(\theta) \tag{4.4}$$

Since f_{ij} are known functions depending on θ the only remaining variable in order to determine the stress field needed is the variable K_I. This variable is denoted the stress intensity factor and is dependent on the applied stress, the crack length and the geometry of the loaded body [16]. The subscript I indicates mode I fracture but solutions for the other modes can be obtained in a similar fashion using different functions depending on the angle, θ.

The stress intensity factor is applied in practice by considering a critical value of this factor upon which cracks will propagate rapidly and failure occurs. This value is called critical stress intensity factor and becomes a measurement of material toughness. The applied stress needed for failure is then dependent of the critical stress

intensity factor, the crack length and the geometric parameter α depending on the crack- and specimen geometry as given in Equation 4.5.

$$\sigma_f = \frac{K_{Ic}}{\alpha\sqrt{\pi a}} \tag{4.5}$$

4.1.3 Non-Linear Fracture Mechanics, NLFM

The NLFM approach is considered for two cases. Either when the plastic zone, described in Section 4.1.2, becomes too large or when the material response is non-linear. The prediction of crack growth can then be obtained either by considering the CTOD-method (Crack Tip Opening Displacement) or the J-integral approach [17].

CTOD

The crack tip displacement, CTOD, approach can be considered both for LEFM as well as for NLFM. In LEFM the CTOD is considered to be zero and can be related to energy release rate, G, as well as the stress intensity factor, K_I. In NLFM it is instead considered as a measurement of the displacement at the crack tip by taking plasticity into account and can be compared to a critical value needed in order for crack growth to occur [17]. Two different approaches for how the CTOD should be used as a crack growth criteria has been derived. Irwin's approach considers an effective crack width as the real crack width plus the length of the plastic zone in front of the crack tip. Dugdale's appraoch considers instead that in order for the stresses to by singular at the crack tip (approaching infinity) the CTOD can not be zero but can be calculated using the length of the plastic zone. For further reading about the COTD approach the reader is referred to [17] and [2]

J-integral

If considering LEFM, the J-integral can directly be interpreted as the energy release rate, i.e. $J = G$, making them equivalent [2]. For NLFM, however, the J-integral can be used in order to some extent determine the equivalent energy release rate when plasticity can't be disregarded and has to be accounted for. It can also be shown that the J-integral is directly related to the CTOD. The parameter J is defined by path-independent contour integrals which in 2-dimensions can be written as given in Equation 4.6. W is the strain energy of the body and T is a tension vector acting perpendicular to the closed contour Γ.

$$J = \int_\Gamma (W \mathrm{d}y - T\frac{\partial u}{\partial x}\mathrm{d}s) \tag{4.6}$$

It can be shown that $J = 0$ along any closed contour following the counter clockwise direction in an arbitrary body in tension. The J-integral is then defined as the change in potential energy along a contour around the crack tip when introducing a crack extension of da in the body. The J-integral is considered a more universal criteria of fracture since for LEFM it can be directly translated to G but also able to

take into account non-linear effects. More reading about the subject can be found in [17] and [2]

4.1.4 Cohesive Zone Modeling, CZM

The theoretical framework for Cohesive Zone Modeling, denoted CZM, were first developed in the 1960s by G.I. Barenblatt and further developed for engineering purposes in the 1970s by A. Hillerborg. The modeling technique is convenient when modeling fracture processes using the finite element method described in Section 4.2 and is implemented in several commercial FE-softwares. The idea of CZM is that a cohesive zone is assumed to exist ahead of the crack tip. The upper and lower surfaces of this zone is held together by cohesive traction stresses which are assumed to decrease as the separation between these surfaces increases, i.e. the crack continues to grow [18]. When the traction stress reaches a value of zero a new crack surface have emerged. An example of a traction-separation relationship for cohesive elements in Abaqus can be seen in Figure 4.2 [5].

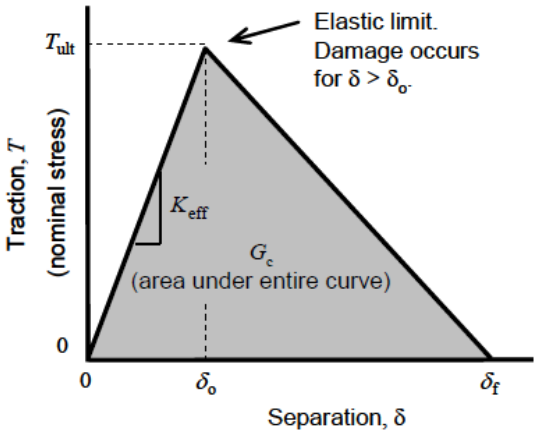

Figure 4.2: Typical traction-separation response using a linear damage evolution law [5]

.

The cohesive zone is, by using the traction-separation response seen in Figure 4.2, modeled as linear elastic defined by a penalty stiffness up until the point of damage initiation. After this point, the material will start to degrade according to a specified damage evolution law, for this case a linear degradation. Cohesive elements are only considered to undergo damage when subjected to tensile or shear loading, according to the modes of fracture described in Section 4.1.1 but not due to compressive loading. The area under the graph can be denoted G_c and specifies the dissipated energy due to failure.

The modeling technique can furthermore be compared to traditional fracture mechanics, described in the previous sections, where crack growth is based only on a critical state at the crack tip and can therefore be seen as a single event. By using CZM this crack growth is rather seen as a process determined by the traction-

separation relationship and is therefore more convenient when using the finite element method for modeling.

Another advantage of CZM is that fracture can be modeled even with the absence of an existing crack in the modeled speciment. A cohesive zone is instead defined where fracture can be assumed to occur. Through the traction-separation relationship crack initiation and crack growth within the cohesive zone can be modeled even without defining an existing crack.

4.2 Finite Element Method

An introduction to the finite element method is described by Ottosen & Persson (1992) [14] as a numerical method for solving differential equations by using approximations. The differential equations that are used to describe the physical behaviour of a body can be solved over very complex geometries in two- or three dimensions by dividing the body into a number of smaller elements called finite elements. By considering approximations of each finite element even highly non-linear behaviour over an entire body can be captured by assuming a polynomial variation over each of these small finite elements. The differential equations that can be solved using the finite element method includes various types of physical behaviour such as flow of heat and fluids, diffusion, electrical currents and elastic behaviour of one-, two- and three dimensional bodies etc..

The polynomial approximation used is an interpolation between certain points to describe the physical variations over the finite element. These points, called nodal points, are usually located at the boundary of a finite element The approximation can be both a linear, quadratic or cubic polynomial and are used to interpolate the variations between these points in a more or less accurate manner depending on the degree of the polynomial.

To perform the approximated interpolation, the nodal points needs to be known. The values of the physical variables in the nodal points, called degrees of freedom, then become unknowns in a linear system of equations. This system of equations have then been discretised into a finite number of equations in contrast to the continuous system before dividing the system into a finite number of elements. The linear system of equations used to solve for the unknown degrees of freedoms can then be described by Equation 4.7.

$$\mathbf{Ka} = \mathbf{f} \tag{4.7}$$

Where $\mathbf{K}$ is the stiffness matrix, describing the constitutive behaviour, i.e. the relationship between physical quantities in the specific body. $\mathbf{a}$ is a vector containing the unknown degrees of freedom and $\mathbf{f}$ is the force vector containing unknown internal forces as well as known forces caused by external effects such as applied force or temperature changes.

To obtain a unique solution to this linear system of equations some degrees of freedom needs to be prescribed, i.e. the physical value at some degrees of freedom are assumed to be known. Further reading about the Finite Element Method can be found by Ottosen & Persson (1992) [14]

4.2.1 Element Types

There exist a number of element types used for different applications in FE-softwares. They can be characterized by the following properties [22]

- Geometry
- Number of degrees of freedom
- Number of nodes
- Formulation
- Integration

Since the behaviour of the element type will vary depending on the properties there are a number of element types that are suitable for different applications. For example there are a number of element types suitable for different geometries of the body to be analysed such as solid continuum elements, shell elements, truss elements, beam elements, etc that can be seen in Figure 4.3. This is only a selection of element types and a number of additional element types can be found and vary between different FE-softwares.

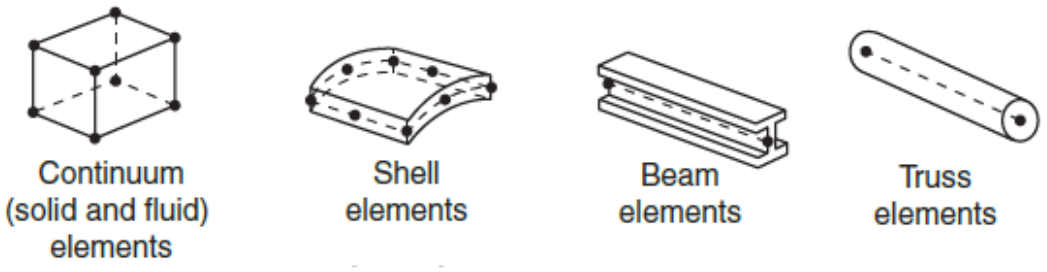

Figure 4.3: A selection of element types used for different FE applications [22]

.

The degrees of freedom for an element are related to the type of analysis that are to be performed. For a stress analysis, for example, the degrees of freedom represents the translation and rotations of the node while in a heat transfer analysis they represent the temperature in the node. Different element types are therefore applicable for different analysis types.

The unknowns at the degrees of freedom are calculated at the nodes of an element. At other points of the element this quantity is interpolated. Stresses and

strains are, however, calculated at material points. The order of interpolation is usually determined by the number of nodes in an element. The number of nodes and the order of interpolation are therefore related. An element with nodes only at the corners of an element, such as the left continuum element in Figure 4.3, employs a linear interpolation and is called a first-order or linear element [22]. If an additional node is inserted between the corner nodes the element will employ a quadratic interpolation and is called a quadratic element or second-order element.

The formulation of an element is related to the mathematical theory that describes the behaviour of the element. Several different formulations can exist for an element type that in other properties are identical such as in geometry, number of nodes and in type of degree of freedom. The different formulations can be more or less suitable for certain applications and can therefore be varied by the user to obtain the desired behaviour of the element for the current analysis.

FE-software also uses different numerical approximations to integrate certain quantities over the volume of each element. Such an approximation is the Gaussian quadrature which is employed for most elements in the computer software Abaqus used in this thesis [22]. The material response is then evaluated at each integration point of the element.

Shell Elements

Shell elements are a certain type of elements which are appropriate for modeling geometries where the thickness is significantly smaller than the the other, in-plane dimensions [22]. Plane stress conditions are therefore assumed for these type of elements. Shell elements can be divided into conventional- and continuum shell elements. Conventional shell elements uses a reference surface to define the geometry and then assigning this reference surface a certain, in comparison small thickness. This type of element will have both translational and rotational degrees of freedom. Continuum shells on the other hand uses a full three-dimensional geometry of the body for discretisation and the thickness of the element is assigned from the geometry. Continuum shell elements only have translational degrees of freedom. The appearance of a continuum shell element will therefore be as for a three-dimensional continuum element but a kinematic and constitutive behaviour similar to a conventional shell element is used instead. The difference between conventional- and continuum shells are illustrated in Figure 4.4.

Cohesive elements

Cohesive elements are a type of special purpose element [22] and are appropriate when modeling the behaviour of for example adhesives, bonded interfaces such as the laminate interface of composites, gaskets or rock fracture. The element type is generally considered when modeling damage and failure in these types of applications. The constitutive relationship can be defined either by using a continuum approach of the material or by defining a traction-separation law to the surface depending on the application area.

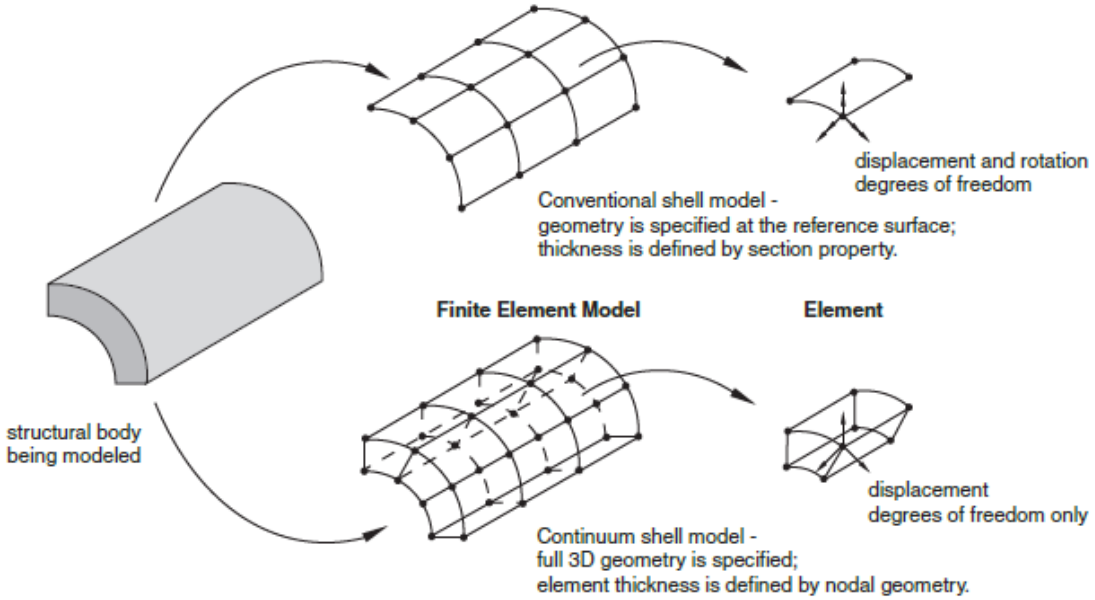

Figure 4.4: Illustration of differences between conventional- and continuum shell elements [22]

.

Cohesive elements use the same connectivity as continuum solid elements and appears geometrically very similar. It is however convenient to think of a cohesive element as a top- and bottom surface separated by a thickness as seen in Figure 4.5. The thickness can either be defined as a constitutive parameter or as the distance between nodal coordinates of the top- and bottom surfaces. These two surfaces therefore needs to be defined when implementing the element type in Abaqus.

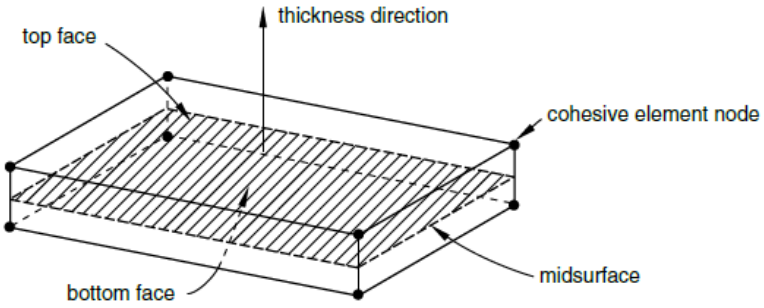

Figure 4.5: Geometry of a cohesive element [22]

.

Continuum-based modeling

The continuum-based approach is usually considered when the adhesive to be modeled can be considered with a finite thickness between the bonded surfaces. The material properties for the adhesive can then simply be defined through normal ma-

terial models with macroscopic stiffness and strength for the material.

Traction-separation-based modeling
The traction-separation-based approach is usually considered when the adhesive layer can be considered as a very thin or even could be considered to be of zero thickness. The mechanical properties of the cohesive elements are then derived from the theory of fracture mechanics and more specifically CZM and the traction-separation relationship described in Section 4.1.4. The method is usually appropriate when modeling delamination of composite materials or failure in other types of adhesive bonds.

The traction-separation relationship can for example be modeled as seen in Figure 4.2 in Section 4.1.4. The constitutive response for the initial elastic behaviour seen in this figure can be described by relating the nominal stress vector, $\mathbf{t}$ (traction vector) to the nominal strain vector, $\boldsymbol{\varepsilon}$ through an elasticity matrix, $\mathbf{E}$ according to Equation 4.8. An uncoupled behaviour between the normal and shear response is for this case assumed. A fully coupled behaviour between the normal and shear response would yield a fully defined elasticity matrix. The nominal strains in this equation are given by dividing the separation with the original constitutive thickness of the cohesive element as seen in Equation 4.9.

$$\begin{bmatrix} t_n \\ t_s \\ t_t \end{bmatrix} = \begin{bmatrix} E_{nn} & 0 & 0 \\ 0 & E_{ss} & 0 \\ 0 & 0 & E_{nn} \end{bmatrix} \begin{bmatrix} \varepsilon_n \\ \varepsilon_s \\ \varepsilon_t \end{bmatrix} \tag{4.8}$$

$$\varepsilon_n = \frac{\delta_n}{T_0},\ \varepsilon_s = \frac{\delta_s}{T_0},\ \varepsilon_t = \frac{\delta_t}{T_0} \tag{4.9}$$

It is furthermore convenient to define the original constitutive thickness as 1.0 to make certain that the nominal strains equals the separations. The elasticity matrix, can then for this case, be defined as the penalty stiffness matrix seen in the traction-separation relationship right away without being scaled first.

The traction-separation response can be defined in a number of ways in Abaqus and allows for a combination of several damage- and failure mechanisms acting on the material at the same time [22]. The traction-separation response is defined by the linear elastic effective stiffness, a damage initiation criteria and a damage evolution law

The damage initiation was, for the purpose of this thesis, defined as the quadratic nominal stress criterion. Damage initiation was then defined by a quadratic interaction function based on the nominal stress in the normal and two shear directions as seen in Equation 4.10.

$$\left\{ \frac{\langle t_n \rangle}{t_n^0} \right\}^2 + \left\{ \frac{t_s}{t_s^0} \right\}^2 + \left\{ \frac{t_t}{t_t^0} \right\}^2 = 1 \tag{4.10}$$

Damage is then initiated if the criteria given in Equation 4.10 reaches a value of 1.

t_n^0, t_s^0 and t_t^0 represents the peak value of nominal stress when deformation is purely acting in one of the three mode directions respectively, i.e. the failure strength of the material in this direction.

The damage evolution law describes the degradation of material stiffness once damage has been initiated. It can either be defined as displacement or by energy. The displacement requires the maximum separation at complete failure, δ_f, to be defined while the energy approach requires the energy dissipated due to failure, G^C, to be defined, i.e. the area under the traction-separation response seen in Figure 4.2. The damage evolution between the point of damage initiation and complete failure can furthermore be defined either as pure linear, quadratic or by user-defined tabular values.

In order to capture the overall effect and combined loading of an element a damage scalar variable, D, is introduced which takes all of this into account. After the initiation of damage, this value will increase from 0 to 1 in a rate dependent on the chosen damage evolution law. The stress components for mode I can then be defined by Equation 4.11. Similar equations exist for mode II in two in-plane shear directions, mode II_s & II_t, but without the second compression criteria. The bar indicates stress components predicted by the elastic stiffness and current strains when damage has not been initiated.

$$t_n = \begin{cases} (1-D)\bar{t}_n, & \bar{t}_n \geq 0 \\ \bar{t}_n, & \text{otherwise (no effect on compressive stiffness)} \end{cases} \tag{4.11}$$

The mix mode behaviour is also specified when defining the damage evolution law and specifies how damage should be evaluated under mixed-mode loading conditions. The relative proportional deformation in the normal and two shear directions is then quantified. This behaviour was for the purpose of this thesis described using a power law. The power law criteria states that an interaction between energies in different modes will occur and together cause failure. The criteria is given by Equation 4.12 where G^C denotes the critical fracture energy required for failure in each respective direction. The variable α constitutes the power factor.

$$\left\{\frac{G_n}{G_n^C}\right\}^\alpha + \left\{\frac{G_s}{G_s^C}\right\}^\alpha + \left\{\frac{G_t}{G_t^C}\right\}^\alpha = 1 \tag{4.12}$$

The material stiffness is then completely degraded and failure occurs when this interaction reaches a value of 1.

5

Analysis of the Overlapping Design

5.1 Introduction

As described in Chapter 3 Marström has proposed a joint design where two structural elements are overlapped and joined together with adhesives. This technique is usually employed by Marström when assembling sail boat masts. A sail boat mast, however, works purely in compression due to the use of stays (a type of pretensioned strut). This is not the case for the Triblade, which was demonstrated in Section 3.3.1. The Triblade will act both in compression, tension and bending depending on which of the three blades that is studied.

Further investigation of this connection type is therefore in the scope of this chapter. Numerical analysis and the FE-software Abaqus was used to study the structural response of this type of connection when subjected to tensile forces, the major force component stressing the adhesive joint. The aim of the study was to determine how different parameters such as the overlapping length and the degree of conical shape over the overlapping length will affect the structural response in the assembled components. From these results an optimum geometry was determined for further studies of the connection.

5.2 Method

The structural components studied in this chapter was based on the prototype made by Marström as discussed in Section 3.2.1. The blade and the plate were not modeled in this study . Only the box spars with an overlapping length were considered. In addition, no regard was taken to the twist incorporated between the blades. Thus, the focus of this study was to investigate how two simple square, hollow-core box spars can be connected using the overlapping technique in an optimized manner by varying certain parameters. Three cases was for this purpose studied. One studying the overlapping length where the cross-section properties remained constant. One studying the conical shape and thereby varying the cross-section properties. Finally a study was carried out where the overlapping length and degree of conical shape were studied at the same time while the cross-section properties remained constant.

The structural response was investigated by studying contour plots of the stress

distribution in the direction of the applied normal force and observing stress concentrations in certain regions. The maximum tensile stress response in the direction of the applied normal force was also compared to the mean stress level in the rest of the structure in order to determine how well the material of the structure was utilized. A variable denoting the stress concentration ratio (SCR) was introduced for this purpose. The SCR was calculated as the maximum stress level in the direction of the applied normal force divided by the stress level in the same direction of an arbitrary element in the region with uniform stress distribution. The ideal condition would be to optimize the structure such that the SCR is equal to one or at least, as close as possible to one. The ideal condition of SCR could be interpreted such that no stress concentrations occur and the stress level is constant through the entire structure.

5.3 Overlapping length

The first parametric study was made to study how the overlapping length affect the stress distribution for an applied tensile normal force.

5.3.1 Geometry

Two simple square, hollow-core beam elements were considered to simulate the box spars. One was inserted into the hollow-core of the other as seen in Figure 5.1. The smaller box spar was set to have an outer dimension of 90x90 mm in order to roughly correspond to the dimensions of the prototype described in Section 3.2.1 and the reference connection described in Section 3.3. The dimensions of the larger box spar was set to 97.4x97.4 mm in order to fit on the outside of the smaller one while also allowing a 0.1 mm gap in between for modeling the adhesive single lap joint. The thickness of both box spars was set to 3.6 mm as seen for the prototype. The cross-sections of each box spar is shown in Figure 5.2. The variable overlapping length denoted, x, in Figure 5.1 was set to 50, 75, 100, 150, 200, 300 and 400 mm.

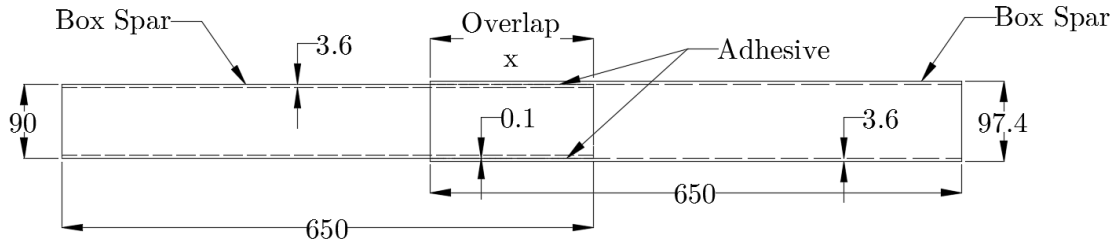

Figure 5.1: Sketch showing the box spars to be studied with varying overlapping length. Dimensions are given in mm.

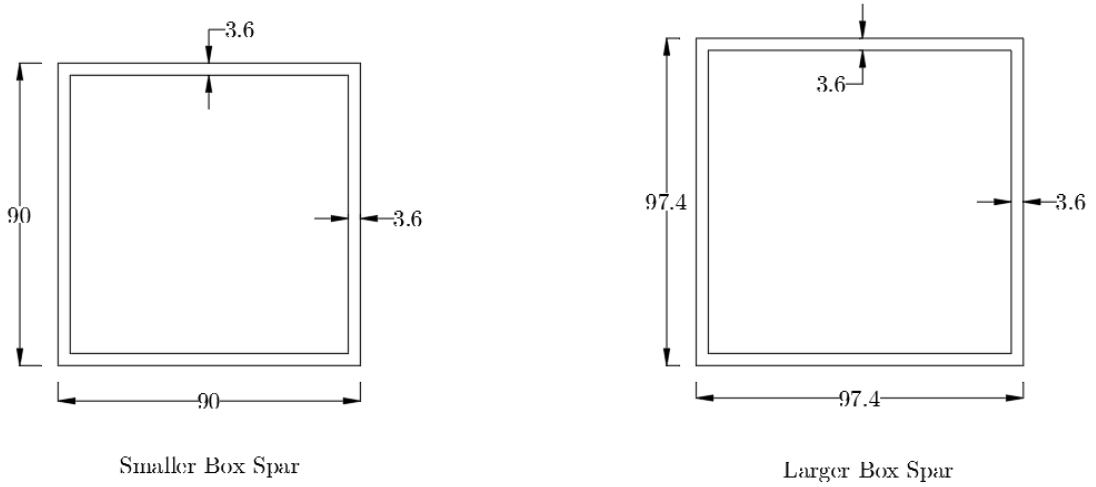

Figure 5.2: Cross-section sketches of the smaller and larger box spar. Dimensions are given in mm.

5.3.2 Material properties

The material properties of the box spars were taken according to the prototype described in Section 3.2.1. As seen in Figure 3.9 the box spars have a different number of layers and orientation of fibres in the flanges compared to the web. The same layered stacking of laminates is investigated in this section and can be seen in Table 5.1.

Table 5.1: Layered stacking of laminates in webs and flanges of the box spars.

Ply	Webs	Flanges
1	Hexply M49 285P	Hexply M49 600 T2x2
2	Hexply M49 285P	Hexply M9.6 UD600
3	Hexply M49 285P	Hexply M9.6 UD600
4	Hexply M49 285P	Hexply M9.6 UD600
5	Hexply M49 285P	Hexply M9.6 UD600
6	Hexply M49 285P	Hexply M49 600 T2x2
7	Hexply M49 285P	-
8	Hexply M49 285P	-
9	Hexply M49 285P	-
10	Hexply M49 285P	-
11	Hexply M49 285P	-
12	Hexply M49 285P	-

The adhesive region in the overlapping section was set to the material parameters of 3M DP490 Epoxy described in Section 3.2.1.

5.3.3 Modeling

The box spars made out of carbon fibre were modeled using composite layups where each of the plies given in Table 5.1 with its individual properties and relative thickness taken into account. The adhesive properties were modeled as an isotropic material with an elastic modulus and Poisson's ratio according to the properties of 3M DP490 Epoxy in Section 3.2.1.

Orientations

Both a global orientation of the structure and a local material orientation for the carbon fibre were assigned to the model. The local material orientation were assigned to the composite layup for each of the box spars such that the 1- and 2-direction were always located in-plane of the layered composite stacking. The local material orientation as well as the global coordinate system can be seen in Figure 5.3. It should be noted that the 1-, 2- and 3-direction could be denoted the x-, y- and z-axis respectively.

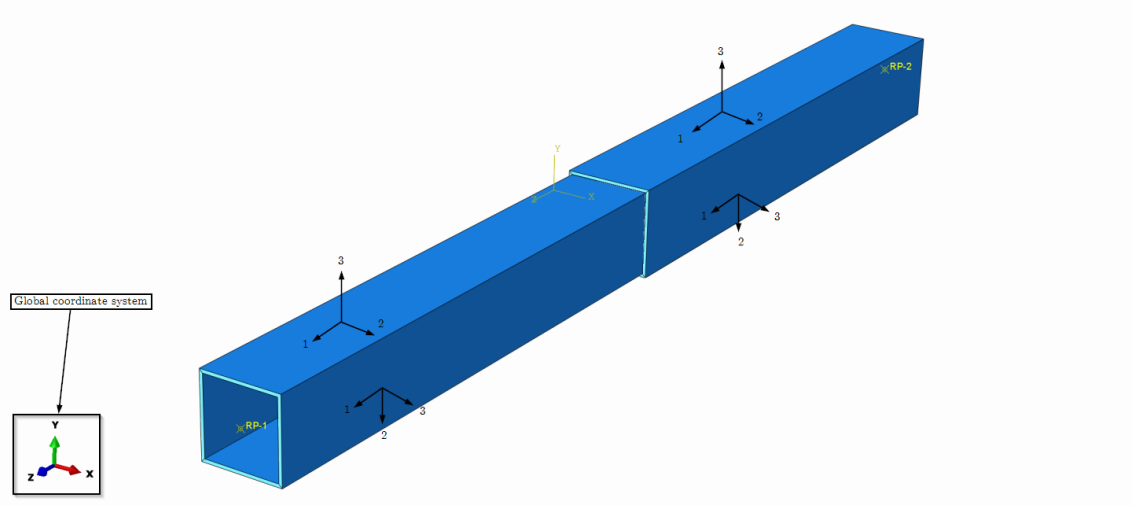

Figure 5.3: Illustration of the global coordinate system of the model as well as the local material orientation directions of the carbon fibre structural elements.

The in-plane stress components for the carbon fibre was therefore given in the 1- and 2-direction of the local material orientation. The 1-directions is given in the direction of the normal force while the 2-direction was given in the transverse direction.

Mesh

The box spars were meshed using linear hexahedral continuum shell elements, denoted as `SC8R` in Abaqus, which were considered appropriate for meshing the composite layups. The adhesive region was meshed using linear hexahedral continuum solid elements, denoted as `C3D8R` in Abaqus.

Constraints

The adjacent surfaces between the adhesive region and the box spars were constrained using a tie constraint. Thus, these surfaces were tied together and unable to move in relation to each other [22].

Each side of the box spars were constrained to a reference point located in the middle of the cross-section using MPC (Multi-Point Constraints). The MPCs tie the cross-section of each box spar to this reference point by connecting them using rigid beam elements [22]. The reference point could then be used for applying the normal force and the boundary condition. Since these points are rigidly connected to the cross-section both the normal force and boundary condition will apply for the entire cross-section even though they are only applied in a single point. The MPC will also enforce the cross-section to be rigid but since there is a large enough distance to the overlap joint, the error is assumed to be negligible. An example of the MPC constraint can be seen in Figure 5.4.

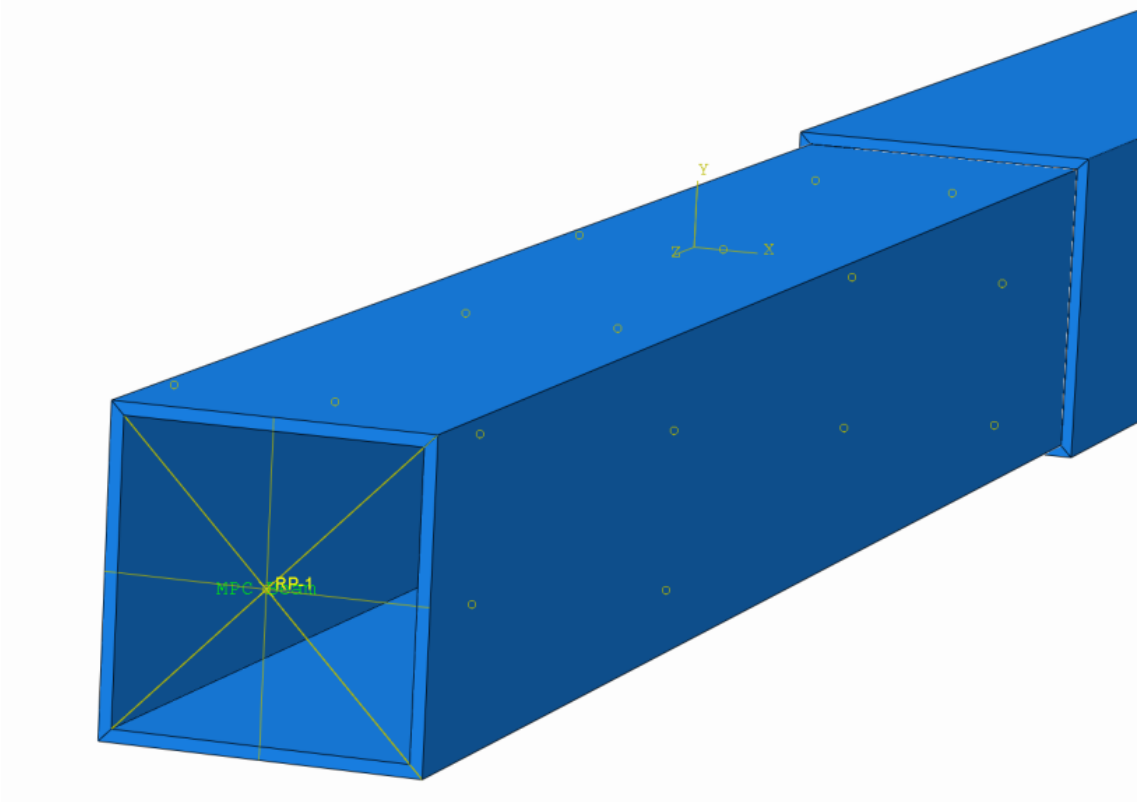

Figure 5.4: MPC constraint used to tie the cross-section to a reference point in the middle using rigid beam elements.

Loads and boundary conditions

The load, aiming to simulate the normal force, was applied at the reference point on the smaller box spar as a concentrated force. The force was applied as the maximum value of the tensile normal force due to aerodynamic- and gravitational loads as

given in Figure 3.13a together with the centrifugal force calculated in Section 3.3.2 as calculated in Equation 5.1.

$$F_{tension} = 17053 + 5869 = 22922 \quad \text{N} \tag{5.1}$$

The structure was constrained from moving by prescribing all translational and rotational degrees of freedom in the reference point of the larger box spar to zero. The applied force and boundary condition at their respective reference point is illustrated in Figure 5.5.

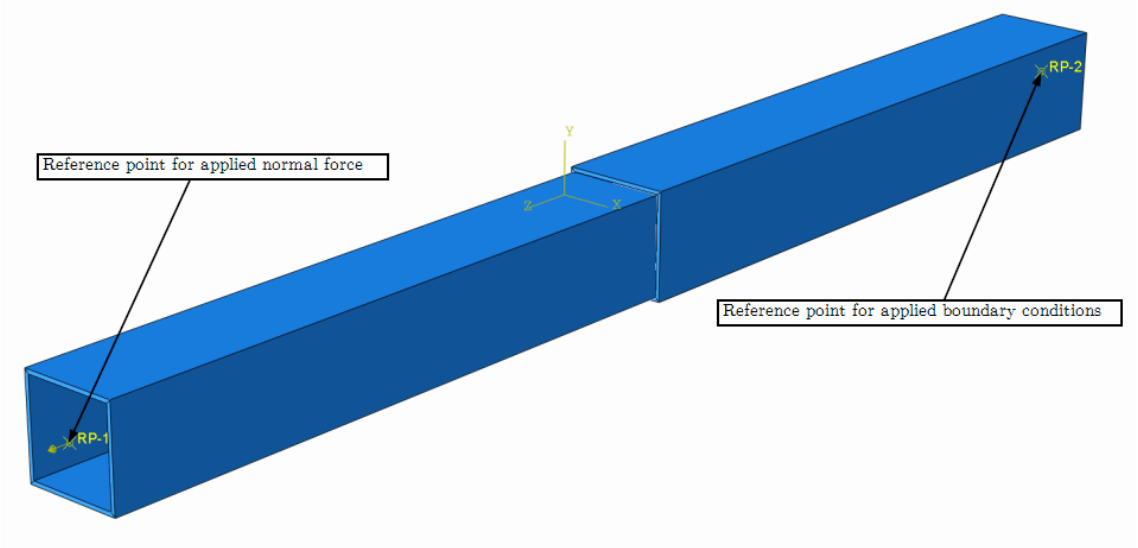

Figure 5.5: Illustration of the reference points used for applying the normal force and boundary conditions respectively.

5.3.4 Results

Contour plots showing the stress distribution in terms of S11, the direction of the applied normal force, in the outermost ply of the carbon fibre can be seen in Figure 5.6. Only two overlapping lengths, 50 and 100 mm, are shown in this figure in order to visualize how the stress distribution can appear and vary in the S11-direction. As can be seen in these figures, there are very high stress concentrations around the ends of the connection. More specifically, the stress concentrations are located where stiffness changes occur in the structure, i.e. at both ends of the overlapping section. This concentration is reduced when increasing the overlapping length and can to some extent be seen when comparing Figure 5.6a to 5.6b where the maximum tensile stress is vastly reduced by increasing the overlapping length.

The green regions in Figure 5.6 where no stress concentrations occurs are subjected to very similar stress values over this entire region. The stress level in these regions remain relatively constant when increasing the overlapping length. An arbitrary finite element is therefore considered in this region when calculating the stress concentration ratio, SCR, as the ratio between the maximum tensile stress and the

tensile stress in this region. This ratio can be seen in Figure 5.7 and serves as a measurement of how well the material in the connection is utilized.

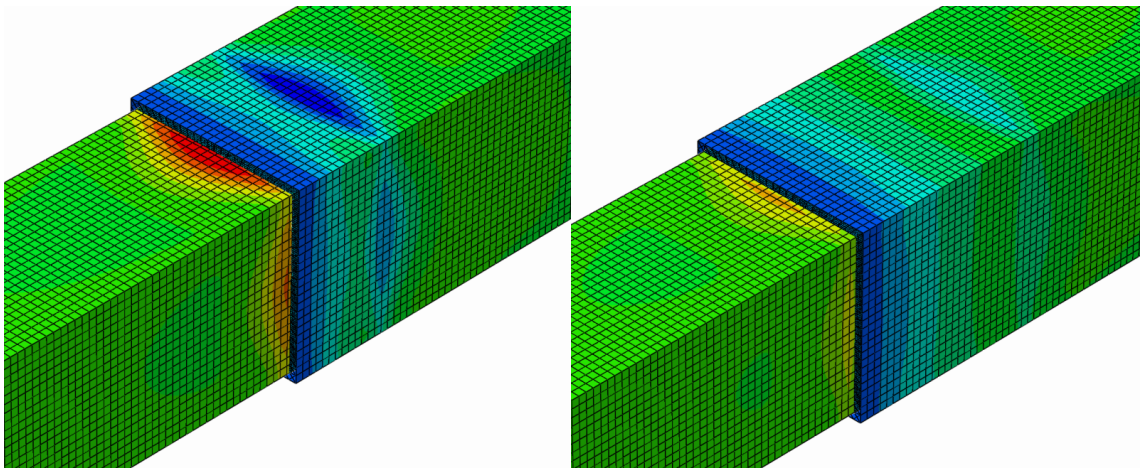

(a) S11 50 mm overlap. **(b)** S11 100 mm overlap.

Figure 5.6: Contour plots showing the S11 stress distribution for an overlapping length of 50 and 100 mm where the contour scale ranges from a minimum of -8.8 MPa (blue) to a maximum of 34.9 MPa (red). (a) S11 50 mm overlap and (b) S11 100 mm overlap.

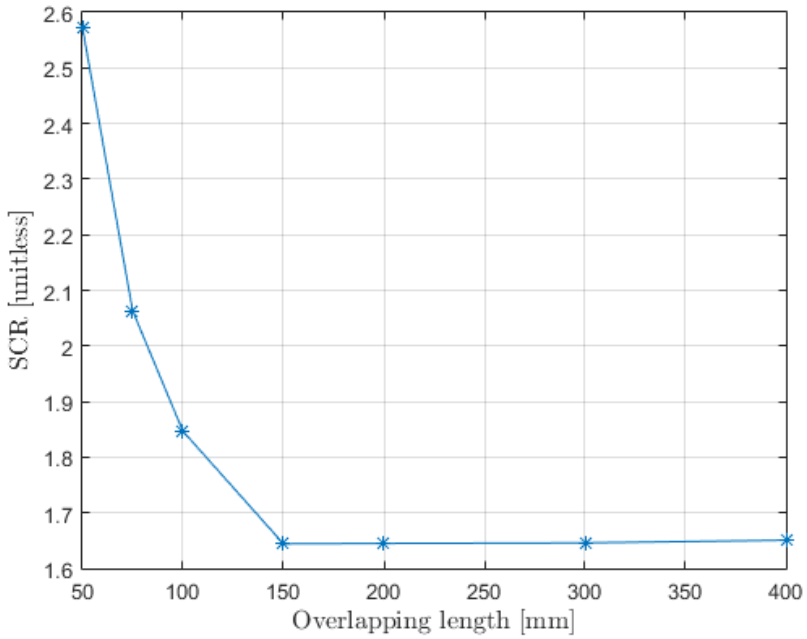

Figure 5.7: Diagram of the Stress Concentration Ratio, SCR, for the maximum tensile stress, S11, as a function of the overlapping length.

5.4 Conical shape of overlap joint

A second parametric study was performed to determine how a conical shape over a constant overlapping length will affect the structural response. The study was very similar to the parametric study of the overlapping length performed in Section 5.3 but with the degree of coning and outer dimensions of the larger box spar as the variable parameter to be studied.

5.4.1 Geometry

The assembled box spars were set to have similar geometric properties as described in Section 5.3. The overlapping length, however, was kept at a constant value of 200 mm since the SCR had leveled out at this overlapping length according to Figure 5.7. The assembled components over the overlapping length can be seen in Figure 5.8. The outer dimensions of the smaller box spar had the same outer dimensions of 90x90 mm while the larger one had a varying outer dimension depending on the degree of coning. The conical shape of the box spars were achieved by linearly decreasing the thickness from 3.6 mm to the variable parameter, x, over the overlapping length as seen in Figure 5.8. An adhesive layer with a thickness of 0.1 mm was still applied in between the structural elements. The adhesive joint could now be considering being a hybrid between the single lap joint and the scarf butt joint seen in Figure 2.2. As the degree of coning is increasing throughout this parametric study a transition from a single lap joint to a scarf butt joint is achieved.

The dimensions of the larger box spar was dependent on the degree of coning and was described by the equation, $90+2x+0.2$, which takes into account the dimension of the smaller box spar, the degree of coning and the adhesive thickness.

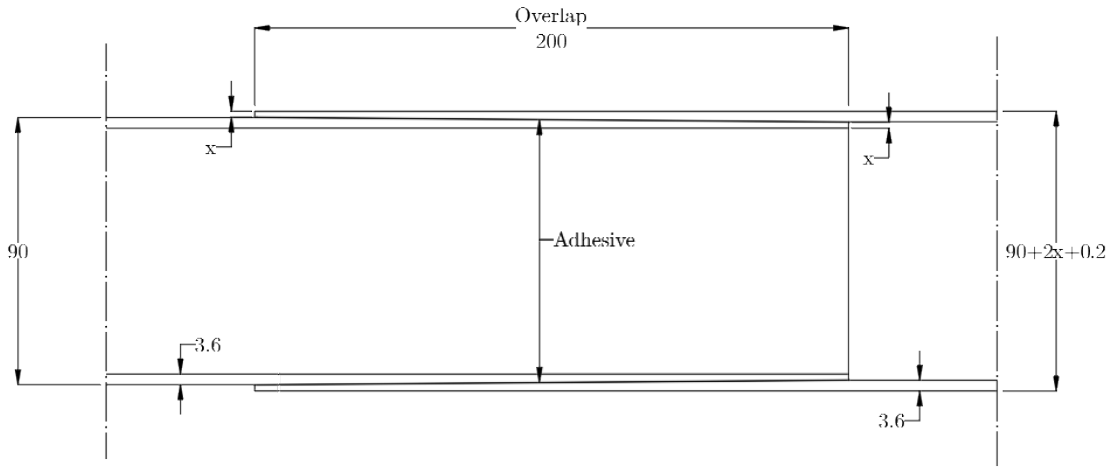

Figure 5.8: Sketch showing the box spars to be studied with varying degrees of coning but a fixed overlapping length of 200 mm. Dimensions are given in mm.

The studied cases with different values of the variable, x, corresponding outer dimension of the larger box spar and the degree of coning can be seen in Table 5.2. The

degree of coning was determined by calculating the inclining angle when reducing the thickness with a certain value over the length of 200 mm.

Table 5.2: Studied cases with the varied parameter, x, the corresponding outer dimensions of the larger box spar and the degree of coning.

Case	x [mm]	Outer dimension $90 + 2x + 0.2$ [mm]	Degree of conical shape [°]
1	3.6	97.4x97.4	0
2	3	96.2x96.2	0.1719
3	2	94.2x94.2	0.4584
4	1	92.2x92.2	0.7448
5	0.5	91.2x91.2	0.8880
6	0.1	90.4x90.4	1.0026

5.4.2 Material properties

The material properties for both the box spars and the adhesive material was constant and set to the values shown in Section 5.3.2. The set-up of the layered laminates was therefore assumed to be constant even over the conical shape. This might not correlate to reality depending on how to conical shape is manufactured but was for the purpose of this study deemed to be sufficient.

5.4.3 Modeling

The modeling procedure was identical to the parametric study of the overlapping length as described in Section 5.3.3. Continuum shell elements and a composite layup was used to model the carbon fibre. Adhesives were modeled as isotropic solid elements. The same orientation, constraints and loads were applied as discussed in Section 5.3.3.

5.4.4 Results

Contour plots showing the stress distribution in the outer most ply of the carbon fibre in terms of S11 for case 2 and case 6 according to Table 5.2 can be seen in Figure 5.9. When comparing Figure 5.9a with 5.9b one can clearly see that the stress concentrations are much higher for case 2 than for case 6. The stress, is for case 6, much more evenly distributed and the maximum stress has been reduced and is more similar to the regions where no stress concentration occurs. This is further emphasized in Figure 5.10 where the SCR, calculated as the maximum tensile stress compared to an arbitrary element where no stress concentrations occur, is plotted versus the degree of coning in the overlapping section.

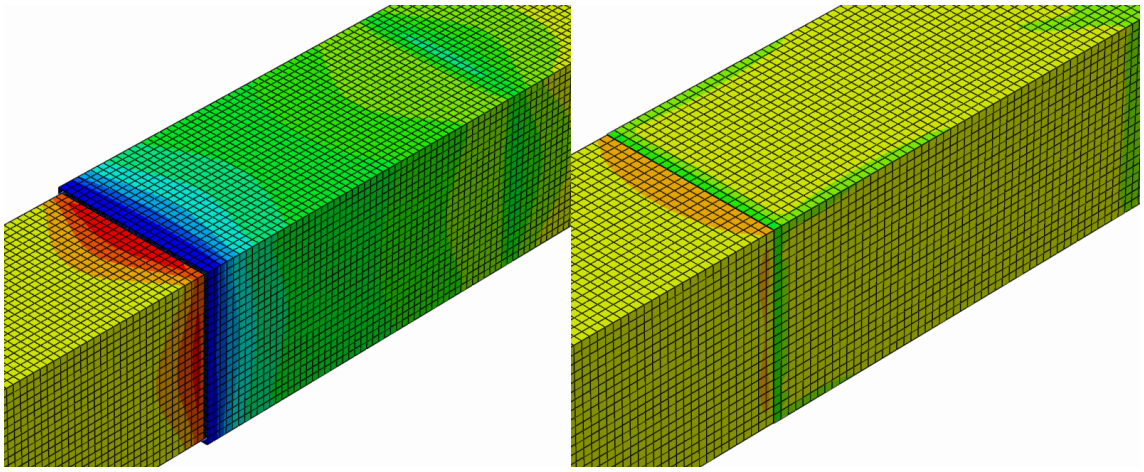

(a) S11 Case 2. **(b)** S11 Case 6.

Figure 5.9: Contour plots showing the S11 stress distribution for case 2 and case 6 where the contour scale ranges from a minimum of -3.4 MPa (blue) to a maximum of 21.3 MPa (red). (a) S11 Case 2, (b) S11 Case 6.

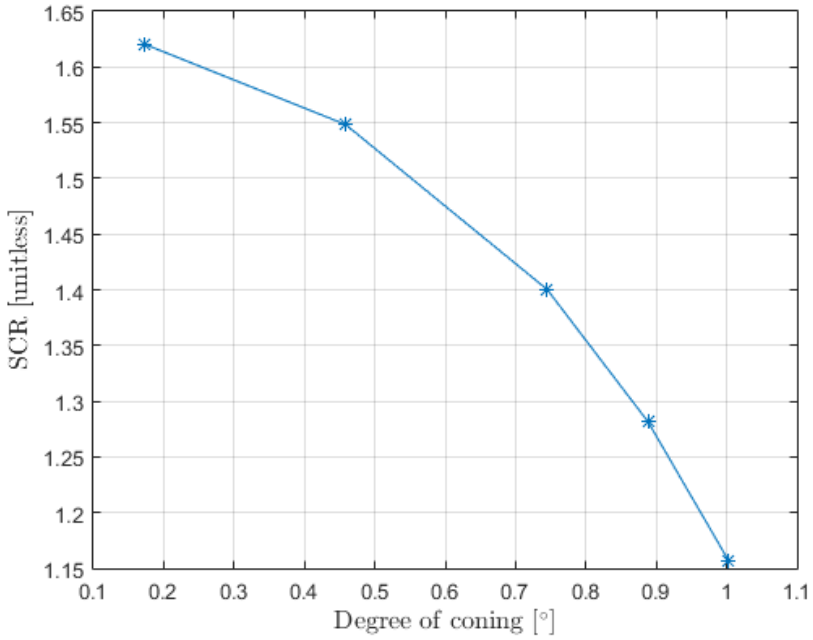

Figure 5.10: Diagram of the Stress Concentration Ratio, SCR, for the maximum tensile stress, S11, as a function of the degree of coning.

5.5 Conical shape and overlapping length

A final parametric study was carried out where both the overlapping length and the conical shape was varied while the cross-section properties of the box spars remained constant. The cross-section properties were given as for case 6 in Table 5.2 since this was determined as the case which best utilized the material in terms of stress

concentrations.

5.5.1 Geometry

The assembled components were set to have an outer dimension as given for case 6 in Table 5.2. The conical shape was then determined by linearly decreasing the thickness from 3.6 mm to 0.1 mm, as seen for this case in Table 5.2, over the varying overlapping length. The joint design could now be seen as a scarf butt joint with varying overlapping length.

A sketch showing the assembled components can be seen in Figure 5.11. Since the thickness was, for all cases, reduced from 3.6 mm to 0.1 mm, a variable overlapping length introduced a variable degree of coning in the assembled components. These parameters can be seen as x and α in Figure 5.11 where; $\alpha = \arctan(\frac{3.6-0.1}{x})$.

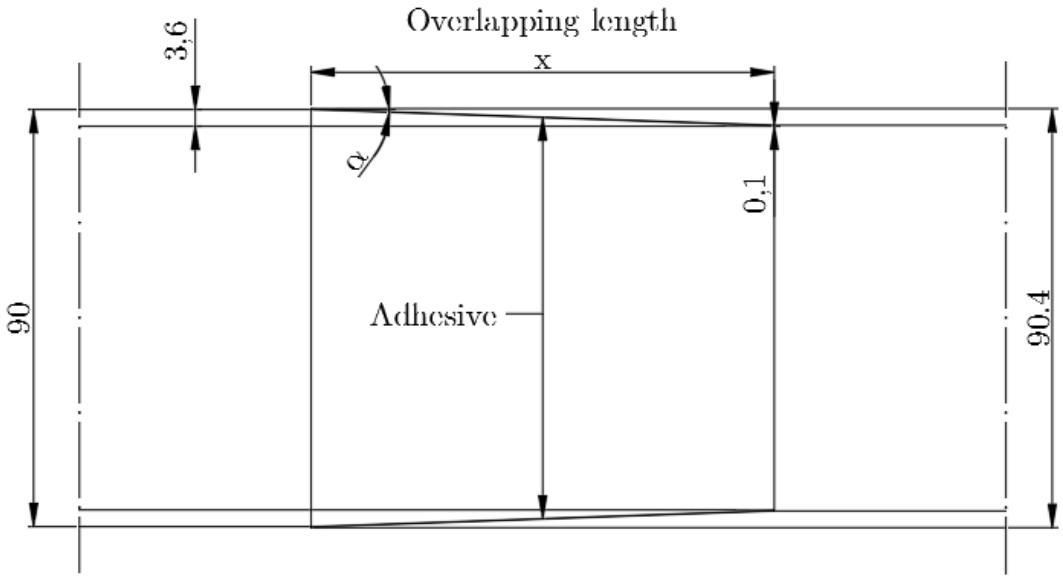

Figure 5.11: Sketch showing the studied box spars with varying degree of coning and overlapping length. Dimensions are given in mm.

The same overlapping lengths as given in Section 5.3 were then considered with varying degree of coning. Table 5.3 shows the studied overlapping lengths and their corresponding degree of coning.
Since the degree of coning was determined by the arctan-function a non-linear variation of the degree of coning over the overlapping length as given in Figure 5.12 can be seen.

Table 5.3: Studied cases of overlapping length with their corresponding degree of coning, α.

Overlapping length, x [mm]	Degree of coning, α [°]
50	4.0042
75	2.6719
100	2.0045
150	1.3367
200	1.0026
300	0.6684
400	0.3342

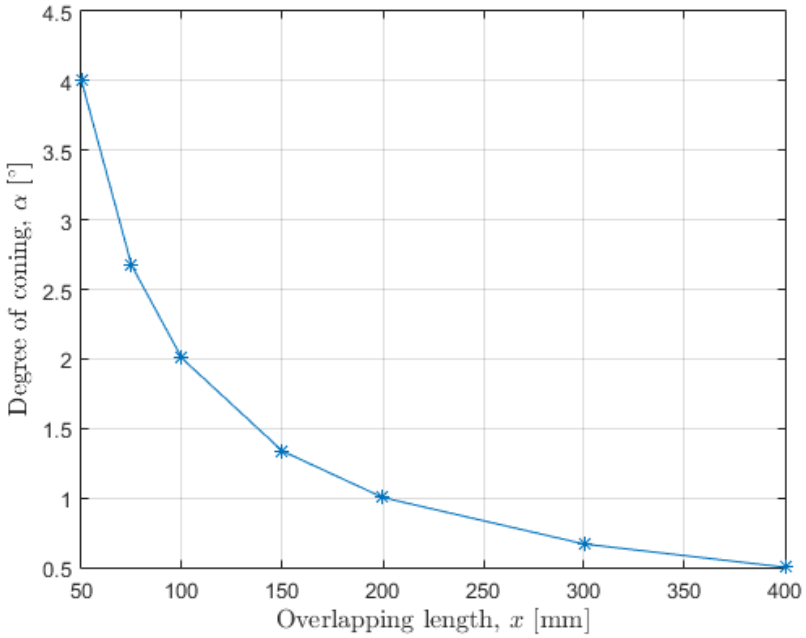

Figure 5.12: The variation of the degree of coning, α, as a function of the overlapping length, x.

5.5.2 Material properties

The material properties for both the box spars and the adhesive material was constant and set to the values shown in Section 5.3.2. The set-up of the layered laminates was therefore assumed to be constant even over the conical shape. This might not correlate to reality depending on how to conical shape is manufactured but was for the purpose of this study deemed to be sufficient.

5.5.3 Modeling

The modeling procedure was identical to the parametric study of the overlapping length as described in Section 5.3.3. Continuum shell elements and a composite layup was used to model the carbon fibre. Adhesives were modeled as isotropic solid

elements. The same orientation, constraints and loads were applied as discussed in Section 5.3.3.

5.5.4 Results

Contour plots showing the stress distribution in the outer most ply of the carbon fibre in terms of S11 for an overlapping length of 50- and 300 mm can be seen in Figure 5.13. Figure 5.13a shows an overlapping length of 50 mm while 5.13b shows an overlapping length of 300 mm. The corresponding degree of coning for these overlapping lengths are given in Table 5.3. When studying and comparing these figures a reduction in the maximum stress level is found with an increase in the overlapping lenght, i.e. a decrease in the degree of coning. The stress is therefore more evenly distributed for an overlapping length of 300 mm compared to 50 mm. This response is further emphasized through Figure 5.14 where the SCR is plotted versus the overlapping length (5.14a) and the degree of coning (5.14b).

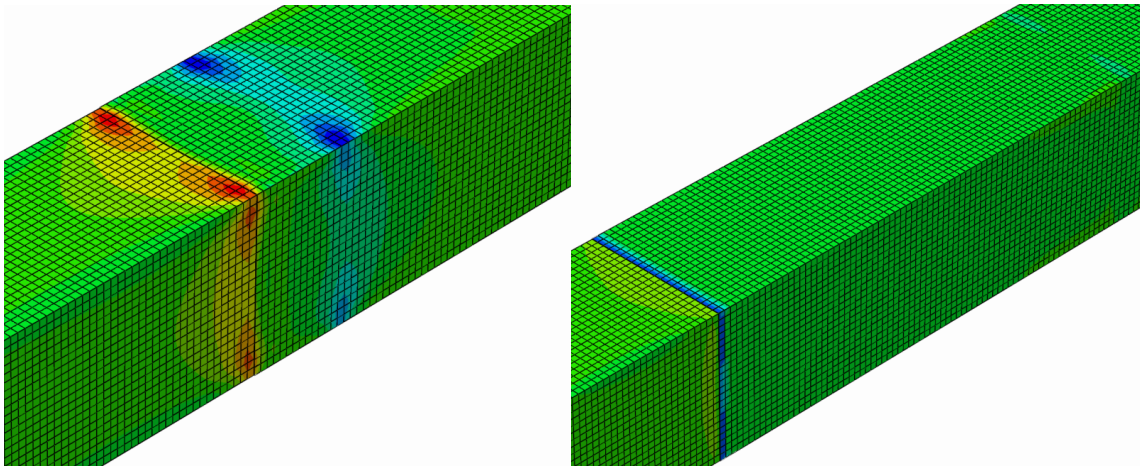

(a) S11 with a conical shape and overlapping length of 50 mm.

(b) S11 with a conical shape and overlapping length of 300 mm.

Figure 5.13: Contour plots showing the S11 stress distribution for a conical shape with an overlapping length of 50- and 300 mm where the contour scale ranges from a minimum of 6.6 MPa (blue) to a maximum of 20.5 MPa (red). (a) S11 50 mm overlap, (b) S11 300 mm overlap.

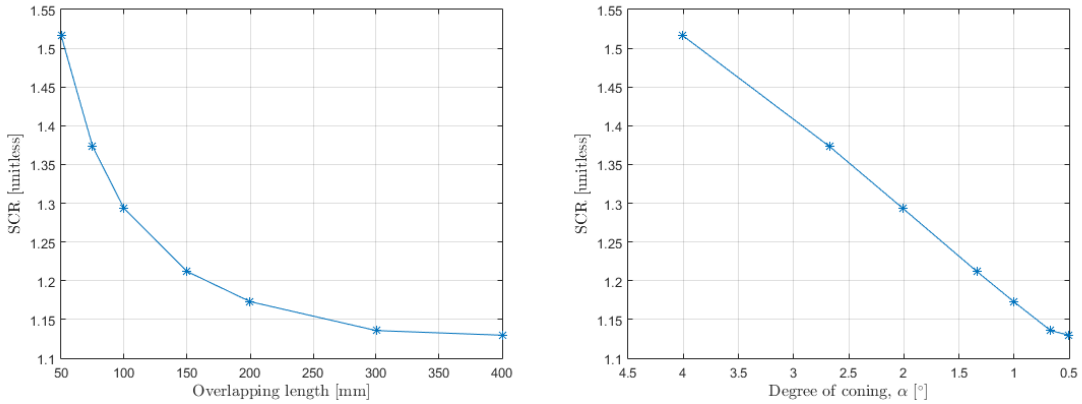

(a) SCR as a function of the overlapping length.

(b) SCR as a function of the degree of coning.

Figure 5.14: Diagram of the Stress Concentration Ratio, SCR, for the maximum tensile stress, S11, as a function of the overlapping length (a) and the degree of coning (b).

5.6 Discussion

Figure 5.7 clearly shows a decrease in the SCR as a function of an increased overlapping length. This decrease is due to a decrease in the maximum tensile stress level with an increased overlapping length. By increasing the overlapping length the maximum stress concentration can be vastly reduced. The variation of the SCR as a function of the overlapping length is non-linear and when the overlapping length has reached a value of 150 mm for this case no further stress reduction is seen. The SCR is reduced from almost 2.6 to around 1.65. This means that for an overlapping length of 50 mm the highest stress is 160% higher than the general stress level while for an overlapping length of 150-400 mm the maximum tensile stress is only 65% higher than the general stress level.

When introducing a conical shape over the overlapping length, and making the transition from a single lap joint to a scarf butt joint, a further reduction in the SCR can also be seen in Figure 5.10. It should be noted that when the overlapping length remains constant, as for this case, and the degree of coning is varied; a change in the outer dimensions of the larger box spar is introduced. This change of outer dimension with a change of degree of coning can be seen in Table 5.2. The stiffness in the overlapping section is therefore changed when increasing the degree of coning. The change in SCR is therefore mainly due to the fact that when increasing the degree of coning, the stiffness change in the structure is also reduced. By examining the results in Figure 5.10 it becomes obvious that a reduced stiffness change in the overlapping section is desired and a very high decrease in stress concentrations can be seen. It appears that the ideal case would be if the cross-section dimensions of both the connecting box spars were identical and a maximum conical shape was introduced over the overlapping length, creating a perfect scarf butt joint. If this

were the case no stiffness change would be introduced over this section and very small stress concentrations would occur. This can be seen for case 6 where the SCR comes very close to the ideal condition since the maximum stress is only around 15% higher than the general stress level.

When studying the results in Figure 5.14a it becomes clear that the SCR is reduced in a very similar manner when varying both the overlapping length and the degree of coning as when only studying the overlapping length as seen in Figure 5.7. The ideal overlapping length, however, seems to be increased and the value of the SCR doesn't seem to be leveling out until an overlapping length of around 300 mm compared to 150 mm when only studying the overlapping length. When studying Figure 5.14b the SCR is linearly decreasing with the degree of conical shape. It then appears obvious that the degree of coning should be minimized in order the reduce the stress concentrations to its maximum. The degree of coning, however, depends on the arctan-function of the overlapping length. This explains why a non-linear change is seen in Figure 5.14a while a linear variation is seen in Figure 5.14b. After a certain overlapping length the degree of coning won't be reduced much further and even though the degree of coning should be minimized an increased overlapping length is unnecessary after a certain point.

The best shape for the overlapping geometry as determined from the parametric studies be selected. The ideal conditions will depend on the overlapping length, the stiffness change and the degree of coning of the structure. Based on this study, the optimum shape was determined as a perfect scarf butt joint with an overlapping length of around 300 mm. This shape was selected when studying the failure behaviour of the adhesive region in the following chapter.

6

Analysis of Failure in the Overlapping Design

6.1 Introduction

The best shape of the overlapping design with regard to stress concentrations based on the parametric studies was found in the previous Chapter 5. This design serves as a base in this chapter where the failure of the adhesive joint is in focus. The adhesive joint failure was modeled using cohesive elements and a traction separation law, as described in Section 4.2.1, by considering two different types of epoxy adhesives. The material properties of one of these adhesives were also varied in order to investigate how the material parameters and different combinations affect the strength and failure of the joint design. Finally, a parametric study was also performed where the shear fracture toughness (critical fracture energy discussed in Section 4.1) and shear failure strength were varied separately to investigate how these parameters affect the load capacity of the joint. The aim of this study was, through modeling, to be able to draw some conclusions regarding the future choice of the adhesive material between connected parts.

6.2 Method

6.2.1 Geometry

The best shape was determined in Section 5.6 as a scarf butt joint with an overlapping length of around 300 mm. For modeling purpose and ease of meshing, however, the degree of coning was chosen as given for case 6 in Section 5.4 where the thickness is reduced from 3.6 mm to 0.1 mm over 300 mm. The use of symmetry was also incorporated in order to reduce computation time. The symmetric quadratic box spar was therefore reduced to a quarter of the original cross-section and symmetry boundary conditions was applied at these edges. The length of the box spars were also reduced in order to further reduce computational time. The adhesive layer was, as previously, modeled with a geometric thickness of 0.1 mm. The reduced model used in Abaqus can be seen in Figure 6.1.

The reference points seen on each side of the box spars in this figure are located in the centre of the original cross-section and are tied rigidly to their respective cross-section. Boundary conditions and loads can therefore be applied in these points,

making them act on the entire cross-section.

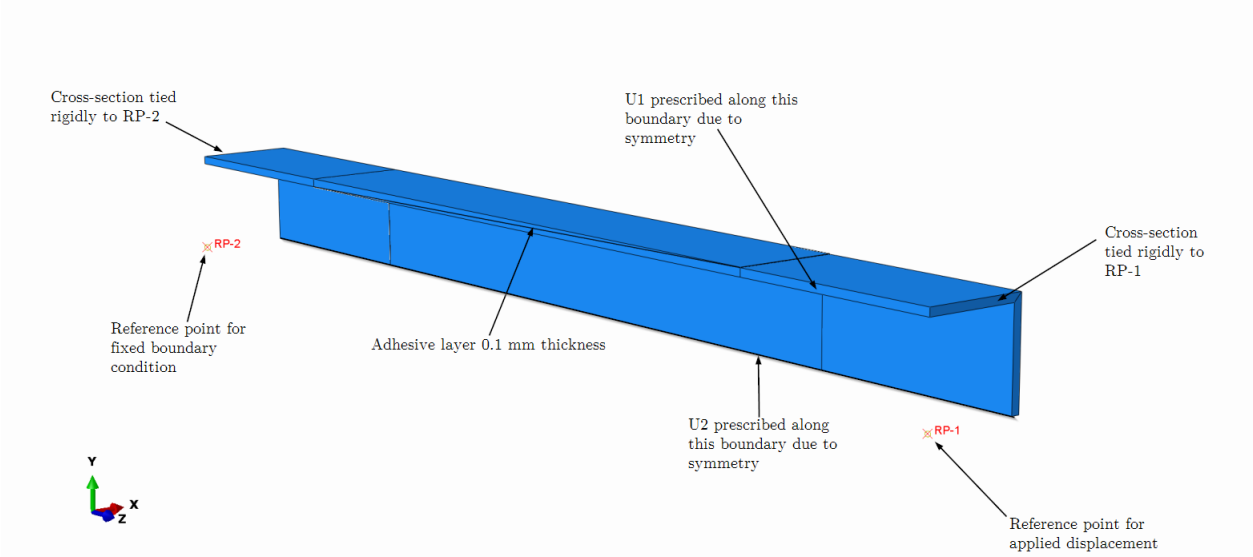

Figure 6.1: Reduced model used in Abaqus for modeling failure.

6.2.2 Material properties

The material properties for the box spars, i.e. the carbon fibre components remained as described in Chapter 5 while the adhesive material 3M DP490 Epoxy was replaced. Two other epoxy adhesives with more extensively known material properties were instead considered as the base for this study. One brittle adhesive, Araldite AV138, and one more ductile adhesive, Araldite 2015 [11]. The material properties for these adhesives needed to define a traction-separation law is shown in Table 6.1.

Table 6.1: Material parameters for Araldite AV138 and Araldite 2015 needed to define a traction separation law.

Property	Araldite AV138	Araldite 2015
Elastic modulus, E [GPa]	4.89	1.85
Shear modulus, G [GPa]	1.56	0.56
Tensile failure strength, σ_f [MPa]	39.45	21.63
Shear failure strength, τ_f [MPa]	30.2	17.9
Fracture toughness in tension, G_I^C [Nm/m^2]	200	430
Fracture toughness in shear, G_{II}^C [Nm/m^2]	380	4700

The traction-separation response can for the two adhesives be given in the normal- and shear directions respectively according to the first two modes of failure given in Section 4.1.1 and can be seen in Figure 6.2. The initial stiffness of these relationships were calculated with the elastic- and shear modulus given in Table 6.1 divided by the assumed thickness of the adhesive layer and can be seen in Table 6.2. As stated

Table 6.2: Effective stiffness values for the traction-separation response for Araldite AV138 and Araldite 2015.

Stiffness	Araldite AV138	Araldite 2015
K_{nn} [N/m]	$4.89 \cdot 10^{13}$	$1.85 \cdot 10^{13}$
$K_{ss} = K_{tt}$ [N/m]	$1.56 \cdot 10^{13}$	$0.56 \cdot 10^{13}$

in Section 6.2.1 the thickness of the adhesive layer was assumed to be 0.1 mm. The shear properties for mode II is furthermore given in two in-plane shear directions which were assumed to be the same and denoted II_s and II_t.

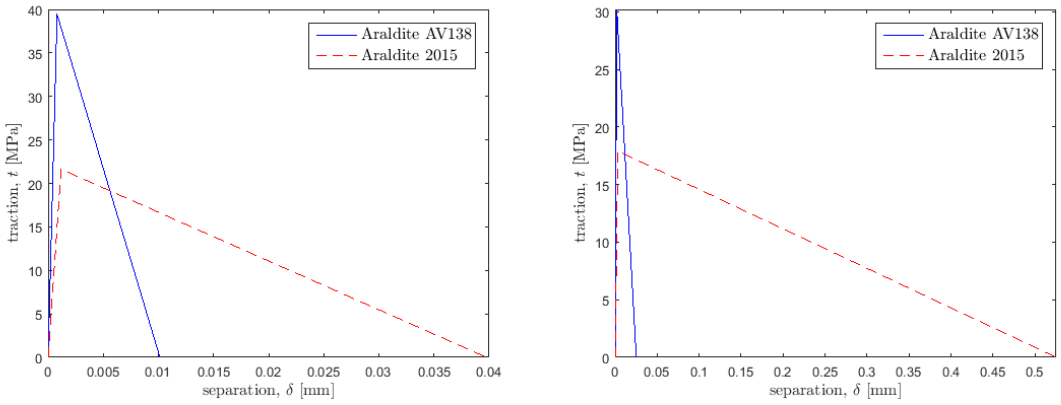

(a) Normal direction, mode I. **(b)** Shear directions, mode II_s & II_t.

Figure 6.2: Traction separation response for Araldite AV138 and Araldite 2015 in the normal and shear directions respectively. (a) Normal direction, mode I, (b) Shear directions, mode II_s & II_t.

The failure strength, ductility and fracture toughness of the adhesives are all related parameters which will effect the failure of the joint. The fracture toughness and failure strength are given as material parameters in Table 6.1. The ductility can be defined as the ability for the adhesive material to deform under loading. This can be described by the separation value at complete stiffness degradation which is considered as the point of complete failure for the traction-separation response. The ductility will therefore relate both to the failure strength and fracture toughness of the adhesive material. A higher ductility is obtained for an adhesive with higher fracture toughness and lower failure strength as the Araldite 2015 while a more brittle adhesive is obtained with higher failure strength and lower fracture toughness as for the Araldite AV138.

6.2.3 Loading and boundary conditions

Since the traction-separation response is highly non-linear displacement controlled loading needed to be applied in order to find a converging solution. A fixed displacement in the global z-direction was therefore applied at RP-1 seen in Figure

6.1 while all other translation- and rotational degrees of freedom were prescribed to zero. The displacement was incrementally applied to the structure until difficulties finding the converged solution occurred. A fixed boundary condition where all degrees of freedom were prescribed to zero was applied in RP-2 seen in Figure 6.1.

6.2.4 Mesh

The carbon fibre parts were as in the previous study meshed using linear hexahedral continuum shell elements, `SC8R`, with an approximate element size of 3.5 mm. The adhesive layer was meshed using hexahedral cohesive elements, `COH3D8` as described in Section 4.2.1. The element size for the cohesive elements was set to approximately 1 mm. For both element types it was of utmost importance to set the stack direction along the element thickness to achieve proper element orientation.

6.2.5 Modeling

The modeling procedure were similar as for the parametric studies in Chapter 5 with the exception that the adhesive material was modeled using cohesive elements. The traction-separation response for these elements were defined through the linear effective stiffness given in Table 6.2. The damage initiation was specified through the quadratic nominal stress criteria and the failure strengths given in Table 6.1. The damage evolution law was described by using an energy approach where linear degradation and a power law criteria with the power of 1 were assumed.

Viscous regularization

The implemented softening behaviour when reducing the material stiffness after damage initiation will introduce high non-linearity to the system [22]. When using Abaqus/standard, an implicit analysis software, convergence issues will arise. Viscous regularization can be used in order to reduce these convergence issues and obtain a more satisfying solution. A viscosity parameter is then introduced in the constitutive equations which allow the tangent stiffness matrix to be positive even in the softening regime for very small time increments. By defining this viscosity parameter as a small value compared to the characteristic time increment the rate of convergence can be improved and the solution can more easily be followed in to the softening regime.

The viscosity parameter was, for the purpose of this study, defined as $1 \cdot 10^{-5}$. This parameter could have beeen further increased in order to get a solution which converged faster around the point of failure, thus making the solution reach further into the softening regime. The effect of this parameter, however, was not studied in detail since it was sufficient to obtain the solution at the point of failure without studying the degradation after this point. Further reading about viscous regularization and its effect on the solution can be found in the Abaqus user's guide [22].

6.2.6 Varying material properties of Araldite AV138

In addition to comparing the two epoxies described in Section 6.2.2 the material parameters of Araldite AV138 were also varied, to some extent, and combined to investigate how the parameters effected the load capacity of the joint. The default values for this epoxy were compared to three other cases. One where the failure strength in both the normal and shear direction was doubled, one where the fracture toughness in both these directions were doubled and one where these two cases were combined. The different cases and the chosen material properties are summarized in Table 6.3. The corresponding traction-separation responses to these cases can be seen and compared to each other in Figure 6.5.

Table 6.3: Varied parameters for Araldite AV138.

Case	Tensile failure strength, σ_f	Shear failure strength, τ_f	Toughness in Tension, G_I^C	Toughness in Shear, G_{II}^C
Araldite AV138 Default	39.45 MPa	30.2 MPa	200 Nm/m^2	380 Nm/m^2
Araldite AV138 $2G^C$	39.45 MPa	30.2 MPa	400 Nm/m^2	760 Nm/m^2
Araldite AV138 $2\sigma_f + 2\tau_f$	78.9 MPa	60.4 MPa	200 Nm/m^2	380 Nm/m^2
Araldite AV138 $2G^C + 2\sigma_f + 2\tau_f$	78.9 MPa	60.4 MPa	400 Nm/m^2	760 Nm/m^2

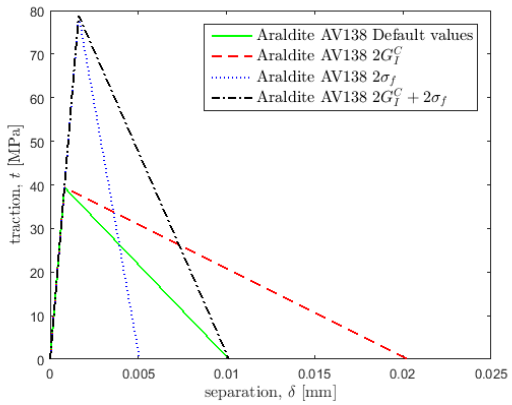

(a) Araldite AV138, normal direction, mode I.

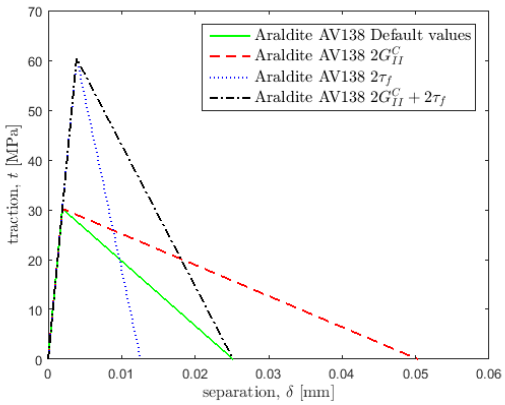

(b) Araldite AV138, shear directions, mode II_s & II_t.

Figure 6.3: Traction separation response with varying material properties for Araldite AV138 in the normal and shear directions respectively. (a) Araldite AV138, normal direction, mode I; (b) Araldite AV138, shear directions, mode II_s & II_t.

It can from this figure also be seen that increasing the fracture toughness will increase the ductility of the adhesive while increasing the failure strength will reduce the

ductility, making it more brittle.

6.2.7 Parametric study of shear fracture toughness and failure strength

A parametric study where the shear fracture toughness, G_{II}^{C}, and the shear failure strength, τ_f, were varied separately while the remaining material properties were held constant was also conducted. These parameters were chosen since both the failure strength and fracture toughness of the adhesive appeared to have a large effect on the load capacity of the joint. The shear direction was chosen due to the fact that the adhesive joint was mainly loaded in shear when applying a tensile normal force. The different parameters studied can be seen in Table 6.4 for the parametric study of the shear fracture toughness and in Table 6.5 for the shear failure strength. All other material properties were remained constant as seen in Table 6.1 for Araldite AV138.

Table 6.4: Parametric study of shear fracture toughness.

Case	Shear fracture toughness G_{II}^{C} [Nm/m^2]
1	100
2	200
3	380
4	500
5	1000
6	1500
7	2000
8	4000
9	6000

Table 6.5: Parametric study of shear failure strength.

Case	Shear failure strength τ_f [MPa]
1	15
2	30.2
3	45
4	60
5	75
6	90
7	105

6.3 Results

A force vs. displacement relationship for RP-1 given in Figure 6.1 were extracted as results from the numerical simulations. A comparison of this relationship for the two investigated adhesives Araldite AV138 and Araldite 2015 can be seen in Figure 6.4 while the relationship for the different variation of parameters for Araldite AV138 discussed in Section 6.2.6 can be seen in Figure 6.5.

Figure 6.6 and 6.7 shows the result of the parametric studies discussed in Section 6.2.7. The resulting peak load at failure of the joint as a function of the shear fracture toughness is given in Figure 6.6 while Figure 6.7 shows it as a function of the shear failure strength in the adhesive.

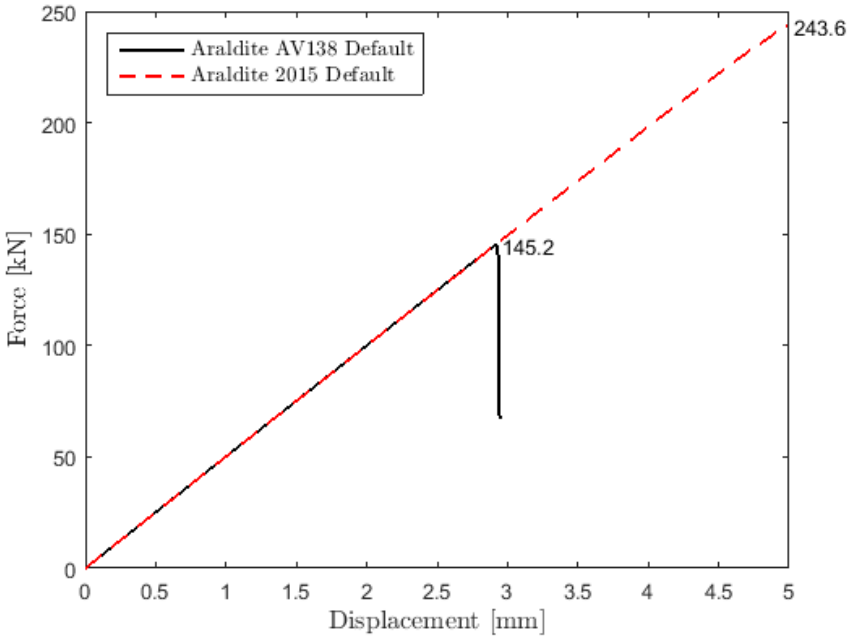

Figure 6.4: Force vs. displacement for the default values of Araldite AV138 and Araldite 2015 respectively.

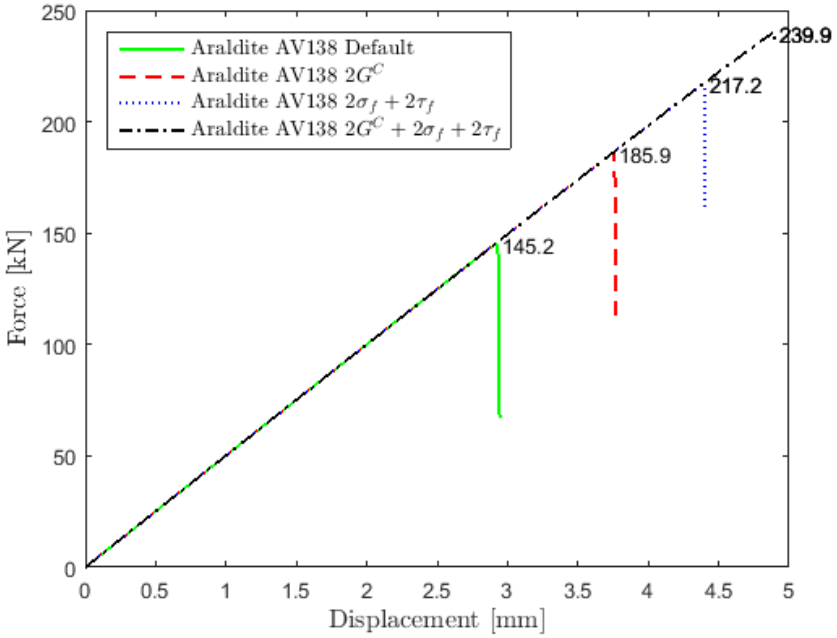

Figure 6.5: Force vs. displacement for the variation of Araldite AV138.

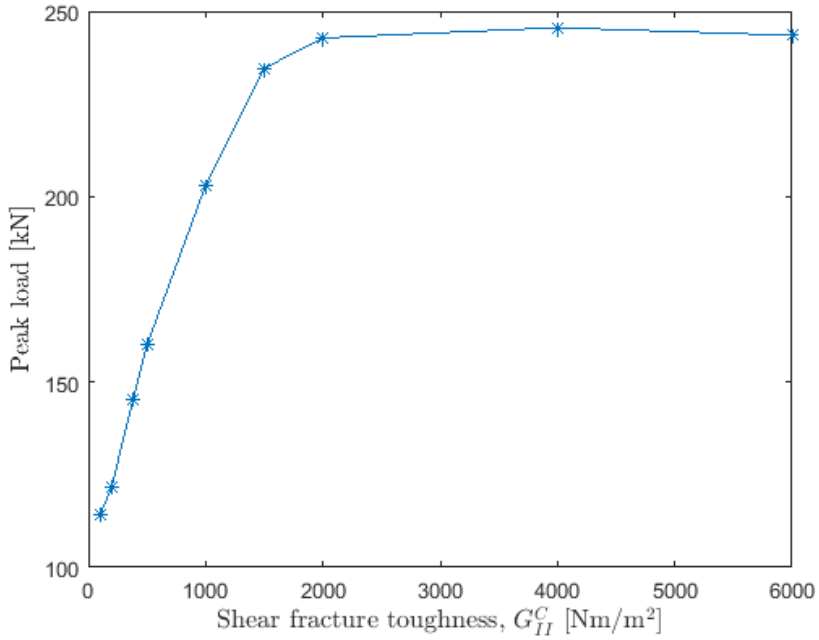

Figure 6.6: Load capacity as a function of the shear fracture toughness of Araldite AV138.

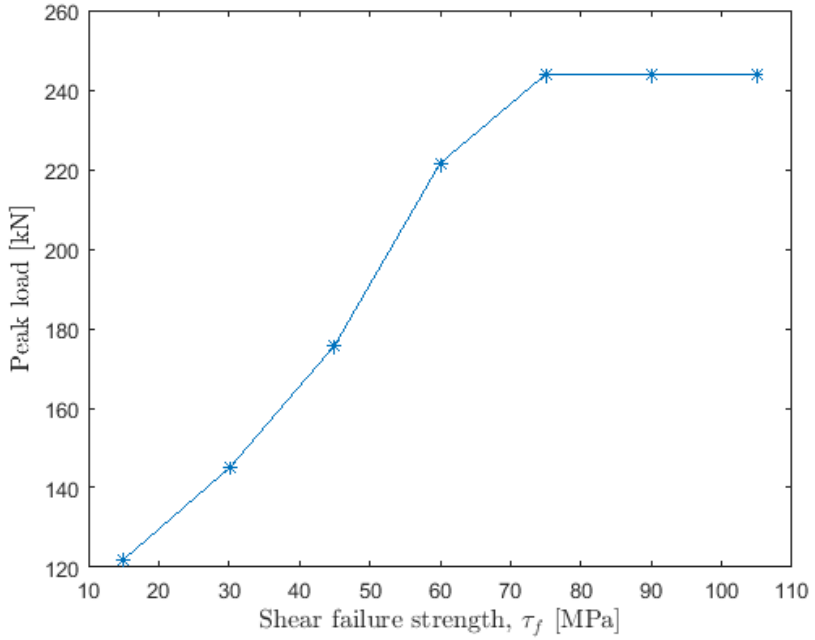

Figure 6.7: Load capacity as a function of the shear failure strength of Araldite AV138.

6.4 Discussion

First of all it could be noted from Figure 6.4 that both the investigated adhesives have sufficient failure capacity with very good margin compared to the applied design load of around 23 kN used when investigating the optimum shape in Chapter 5. Only around 10% of the capacity for Araldite 2015 is utilized while 16% of the capacity is utilized for Araldite AV138. This design load case, however, is very simplified. When scaling up the blades and considering more complex load cases it could be of more important interest to utilize the full capacity of the adhesive material.

The results from the parametric studies in Figure 6.6 and 6.7 suggests that increasing the shear failure strength and the shear fracture toughness separately will increase the load capacity of the joint. This is further emphasized in Figure 6.5 which also suggests that these two parameters are additive, i.e. increasing both values simultaneously will increase the load capacity even further.

This indicates that both these parameters should be as high as possible to maximize the load capacity of the joint. While this statement is true some other aspects can be taken into account. If the results in Figure 6.4 is once again considered it can be noted that the load capacity for Araldite 2015 is 68% higher than the load capacity for the default values of Araldite AV138. Araldite 2015 has a somewhat lower failure strength than the default value of Araldite AV138 but the shear fracture toughness is significantly higher. This suggests that a lower failure strength of an adhesive can be accepted and compensated for if the fracture toughness is high enough, i.e. the adhesive is more ductile. This is the case for most adhesives where the ductility usually comes at the cost of lower stiffness and failure strength. From Figure 6.4 it can be concluded that for this case the more ductile adhesive Araldite 2015 gives a more robust joint design than the Araldite AV138. If the failure strength, however, is too low a lower load capacity might be obtained.

The reason why a ductile adhesive with a lower failure strength could perform better than a brittle adhesive with higher failure strength can be explained by stress concentrations at the edges of the adhesive joint [12]. For a joint, such as the investigated one, stress concentrations will mainly occur at these edges. If a brittle adhesive is used, stress concentrations will remain at the edges. After the point of damage initiation, failure will occur rapidly and uncontrolled crack growth is obtained making the entire joint fail. The slow rate of degrading stiffness in a ductile adhesive, however, will allow for stresses to redistribute in the adhesive material. The adhesive material in the entire joint can therefore be better utilized and contribute to the strength of the joint while for a brittle adhesive only the material at the edges may carry any stress before uncontrolled crack propagation occurs.

It could furthermore, from the results of the parametric study seen in Figure 6.6 and 6.7, be noted that a maximum capacity of the joint can be obtained. After increasing the shear fracture toughness to around 2000 Nm/m^2 or the shear failure

strength to around 75 MPa no further increase of load capacity is obtained. This indicates that excessive values of these parameters won't result in a greater capacity of the joint.

7
Final Remarks

7.1 Conclusions

The use of an adhesive joint to connect the structural elements of a blade through the plates can be a very good solution if done in a proper way. It can be advantageous compared to mechanical fasteners since stress concentrations can be reduced and the material is better utilized. With a proper choice of the adhesive material a very high failure load can also be obtained. It will also help creating a more lightweight structure which is one of the main goals of the Triblade. Some disadvantages with adhesive joints is the controlled environment needed when curing the adhesives and maintenance issues such as inspecting and repair of the Triblade.

Special care should be taken if the adhesive design discussed in this thesis is used to connect modular elements of the Triblade such that stress concentrations are minimized. This is done by avoiding abrupt changes in stiffness at the connection. This can be achieved by employing a conical shape of the box spars in the overlapping section such that the cross-section dimensions are held relatively constant over the connection. The conical shape should be maximized such that thickness is linearly reduced to zero, or as close to zero as possible allowed by manufacturing processes in the overlapping section. This creates a joint very similar to the scarf butt joint seen in Figure 2.2.

The overlapping length of the scarf butt joint should furthermore be maximized such that the inclination of the linear reduction of thickness is as low as possible creating a smooth transition over the connection. The ideal condition would be an infinite overlapping length where the degree of coning approaches zero. The degree of coning, however, is dependent on the arctan-function which makes it approaching zero very fast for small increases in the overlapping length at first. At increased overlapping lengths the degree of coning will change slowly making further increase in the overlapping length unnecessary. A degree of coning of around 0.5-1.0° was shown to be enough to satisfyingly reduce the stress concentrations.

If the above considerations are fulfilled a connection where the stress distributions are very uniform can be achieved providing for a very good utilization of the material in the Triblade.

The failure strength of the adhesive joint can be described by two properties in

the adhesive material. Both the strength of the material and the toughness. These properties are given in three directions, also referred to as modes described in Section 4.1.1. One in the normal direction and two in different shear directions. The joint of focus is mainly subjected to forces in the second mode direction, i.e. one of the shear directions. The shear failure strength and shear toughness in this direction is therefore of largest importance when choosing an adhesive material for the joint. It was shown that a high failure strength and high fracture toughness will yield a robust and strong joint design. However, it was also shown that a lower failure strength can be compensated for if the fracture toughness is significantly high, i.e. a more ductile adhesive is used. This is due to the fact that stresses will redistribute better in a ductile adhesive making for a better utilization of the entire adhesive joint. Therefore, a more ductile adhesive is preferred compared to a brittle and will yield a higher load capacity.

Based on the results of this report it can be recommended that the connection in focus should be designed as a scarf butt joint with an overlapping length of around 300 mm. The stress levels could be further reduced by a small amount by increasing this overlapping length. An overlapping length of 300 mm is recommended though since a longer overlapping length would give very small improvements but require more material as well as making the manufacturing more difficult.

7.2 Further work

It should be emphasized that this thesis has only considered the single overlap design using adhesives suggested by Marström by only applying a tensile normal force. This solution might not be the final design used for the Triblade but the knowledge obtained could be used for similar adhesive joint designs not only in the Triblade but for connection of other carbon fibre parts as well.

Further work on this adhesive connection in the Triblade should include but are not limited to:

- Consideration of all acting loads according to Figure 3.13.
- Including struts in the joint design.
- Considering effects of scaling up the size of the blade and therefore also the connection size.
- Considering how the connection could be designed when implementing different size between sections and twisting of blades in relation to each other.
- Take into account the strength of the adherends, i.e. the carbon fibre components. If the joint is properly designed according to the findings of this report, the adhesive joint could very well have a higher strength than the adherends.
- Investigate how the adhesive joint should be manufactured in reality, i.e. what parameters needs to be controlled during curing in order to manufacture a high quality adhesive joint.
- Experimental testing of the adhesive joint.

Bibliography

[1] Austrell, P-E; Dalblom, O; Lindemann, J; Olsson, A; Olsson, K-G; Persson, K; Petersson, H; Ristinmaa, M; Sandberg, G; Wernberg, P-A. (2004). *CALFEM: A Finite Element Toolbox, Version 3.4*. Lund: Division of Structural Mechanics at Lund University.

[2] Broek, D. (1982). *Elementary engineering fracture mechanics*. The Hague: Martinus Nijhoff.

[3] Brøndsted, P., & Nijssen, R. P. (2013). *Advances in wind turbine blade design and materials*. Philadelphia, PA: Woodhead Publishing.

[4] Burton, T., Jenkins, N., Sharpe, D., & Bossanyi, E. (2011). *Wind Energy Handbook*. Chichester, West Sussex: John Wiley & Sons.

[5] Diehl, Ted. (2004). *Modeling Surface-Bonded Structures with ABAQUS Cohesive Elements: Beam-Type Solutions*. 2004 ABAQUS Users' Conference.

[6] Ebnesajjad, S. (2008). *Adhesives technology handbook*. Norwich, NY: William Andrew Pub.

[7] Estrada, Hector, and Luke S. Lee. "FRP Composite Constituent Materials". *The International Handbook Of FRP Composites In Civil Engineering*. Manoochehr Zoghi. 1st ed. Boca Raton: Taylor & Francis Group, 2014.

[8] Estrada, Hector, and Luke S. Lee. "Mechanics of Composite Materials". *The International Handbook Of FRP Composites In Civil Engineering*. Manoochehr Zoghi. 1st ed. Boca Raton: Taylor & Francis Group, 2014.

[9] Hansen, M. O. (2008). *Aerodynamics of Wind Turbines*. London: Earthscan.

[10] Jain, P. (2011). *Wind energy engineering*. New York: McGraw-Hill.

[11] Lopes, R., Campilho, R., Silva, F. D., & Faneco, T. (2016). *Comparative evaluation of the Double-Cantilever Beam and Tapered Double-Cantilever Beam tests for estimation of the tensile fracture toughness of adhesive joints*. International Journal of Adhesion and Adhesives, 67, 103-111: `http:`

//www.sciencedirect.com/science/article/pii/S0143749615002353

[12] Meredith, H. J., & Wilker, J. J. (2015). *The Interplay of Modulus, Strength, and Ductility in Adhesive Design Using Biomimetic Polymer Chemistry.* Adv. Funct. Mater. Advanced Functional Materials, 25(31), 5057-5065. doi:10.1002/adfm.201501880

[13] Nhamoinesu, S., & Overend, M. (n.d.). *The Mechanical Performance of Adhesives for a Steel-Glass Composite Façade System* (Tech.). Retrieved April 10, 2016, from University of Cambridge, UK website: http://www.gft.eng.cam.ac.uk/media/sn/the-mechanical-performance-of-adhesives-for-a.pdf

[14] Ottosen, N. S., & Petersson, H. (1992). *Introduction to the finite element method.* New York: Prentice Hall.

[15] Park, S. (2015). *Carbon Fibers.* New York: Springer.

[16] Roylance, David. (2001). *Introduction to Fracture Mechanics.* Cambridge, MA: Department of Materials Science and Engineering Massachusetts Institute of Technology.

[17] P.J.G. Schreurs. (2013). *Fracture mechanics Lecture notes - course 4A780.* Eindohoven: Department of Mechanical Engineering at Eindhoven University of Technology.

[18] Stigh, U., Alfredsson, K. S., Andersson, T., Biel, A., Carlberger, T., & Salomonsson, K. (2010). *Some aspects of cohesive models and modelling with special application to strength of adhesive layers.* Int J Fract International Journal of Fracture, 165(2), 149-162. doi:10.1007/s10704-010-9458-9

[19] Sun, C. T., & Jin, Z. (2012). *Fracture mechanics.* Waltham, MA: Academic Press.

[20] Weddig, B. (2016). *Structural Analysis of Truss Construction for Wind Turbine Blades.* Lund: Structural Mechanics, Lund University.

[21] Zehnder, A. T. (2012). *Fracture mechanics.* London: Springer Science Business Media.

[22] *Abaqus 6.14 Analysis User's Guide.* (2014). Dassault Systèmes.

[23] *Airfoil plotter (sg6043-il).* (n.d.). Retrieved April 7, 2016, from http://airfoiltools.com/plotter/index?airfoil=sg6043-il

[24] *Assessment of Research Needs for Wind Turbine Rotor Materials Technology.* (1991). Washington, D.C.: National Academy Press.

[25] *EN 61400-2:2006: Wind Turbines - Part 2: Design Requirements for Small Wind Turbines.* (2006). British Standards.

[26] *Guidelines for Design of Wind turbines.* (2002). Copenhagen: Det Norske Veritas and Risø National Laboratory.

[27] *Mechanical Properties of Carbon Fibre Composite Materials, Fibre / Epoxy resin (120°C Cure).* (n.d.). Retrieved April 10, 2016, from `http://www.performance-composites.com/carbonfibre/mechanicalproperties_2.asp`

[28] 3M. (1996). *Scotch-Weld EPX Adhesive DP490* [Brochure]. United Kingdom.